PERGAMON

Journal of Structural Geology 24 (2002) 247–275

JOURNAL OF STRUCTURAL GEOLOGY

www.elsevier.com/locate/jstrugeo

Modeling of grabens extending above evaporites in Canyonlands National Park, Utah

D.D. Schultz-Ela*, P. Walsh

Bureau of Economic Geology, The University of Texas at Austin, Austin, TX 78713, USA

Received 31 August 2000; revised 19 April 2001; accepted 3 May 2001

Abstract

Grabens in Canyonlands National Park, Utah, began extending above a layer of evaporites when the Colorado River cut through the overburden. Two-dimensional finite element models simulate the effects of geometry and rock properties on graben configuration and spacing. Only those models having a progressively increasing slope or no slope mimicked the natural upslope graben propagation. Typical rock properties produced the most realistic fault patterns: an initial friction angle of 31°, a cohesion of 1 MPa, and strain weakening comprising cohesion loss and decrease of friction angle to 26°. A tensile stress limit narrowed the grabens and reproduced the vertical upper portion of the natural faults. The viscous salt resisted overburden spreading and controlled its rate. Modeled grabens spread at typical rates of 1–2 mm a^{-1} for a salt viscosity of 1×10^{18} Pa s, and the entire system strained at rates from 6.0×10^{-14} s^{-1} to 0.5×10^{14} s^{-1}. The faults bounding a graben formed nearly simultaneously at the top surface and propagated downward. Salt rose beneath the grabens as reactive diapirs. Overburden adjacent to the canyon flexed as salt was expelled and formed an arching horst and graben. A corresponding horst has been found in the field. The model results scale to larger dimensions, except for the steep upper part of the faults. Reduced dimensions create vertical or no faults.

Keywords: Grabens; Salt tectonics; Extension; Finite element analysis; Canyonlands National Park

1. Introduction

The Grabens area of Canyonlands National Park, Utah, comprises an arcuate array of spectacularly exposed normal faults, most of which combine to form grabens (Fig. 1). These grabens began forming in the last 1.4 million years or less. They are still growing by gravity-driven extension downdip toward the Colorado River canyon. Underlying evaporites provide a detachment layer, and the canyon erosion removed the restraints to spreading of the overburden. Deformation of the grabens presumably represents an early stage of extension above salt that has progressed much farther in places such as the Angolan margin (Lundin, 1992). The Grabens area also provides insights into many other systems in which a brittle layer extends above a ductile layer.

The Grabens fault system represents an exceptional opportunity to study the mechanics of gravity-driven deformation above a ductile layer. That recent deformation has been little modified or obscured by erosion and deposition; the geometry and timing are relatively simple and well constrained; and the mechanical properties of the deforming rocks did not change by compaction or lithification. We have simulated the evolution of the grabens using finite-element methods. The restricted number and range of variables in the models allow good inferences to be made about factors that control properties such as the width and spacing of grabens. In addition, the models suggest resolutions to debates that have been difficult to resolve in the field.

The major questions addressed by this study are: (1) what properties determine the dip, spacing and relations of normal faults defining the grabens; (2) what are the geometry and behavior of the graben tips near the salt contact; (3) how do the faults propagate through the rock layer; and (4) how does the salt flow interact with the extending overburden; that is, does the salt flow drive or resist the extension?

To simulate natural behavior accurately, a finite-element code must include realistic constitutive models. The simulations described here used a viscoelastic rheology for the evaporites. A non-associated elasto–plastic rheology

* Corresponding author. Tel.: +1-512-471-4335; fax: +1-512-471-0140.
E-mail address: schultzelad@mail.utexas.edu (D.D. Schultz-Ela).

0191-8141/01/$ - see front matter
PII: S0191-8141(01)00066-9

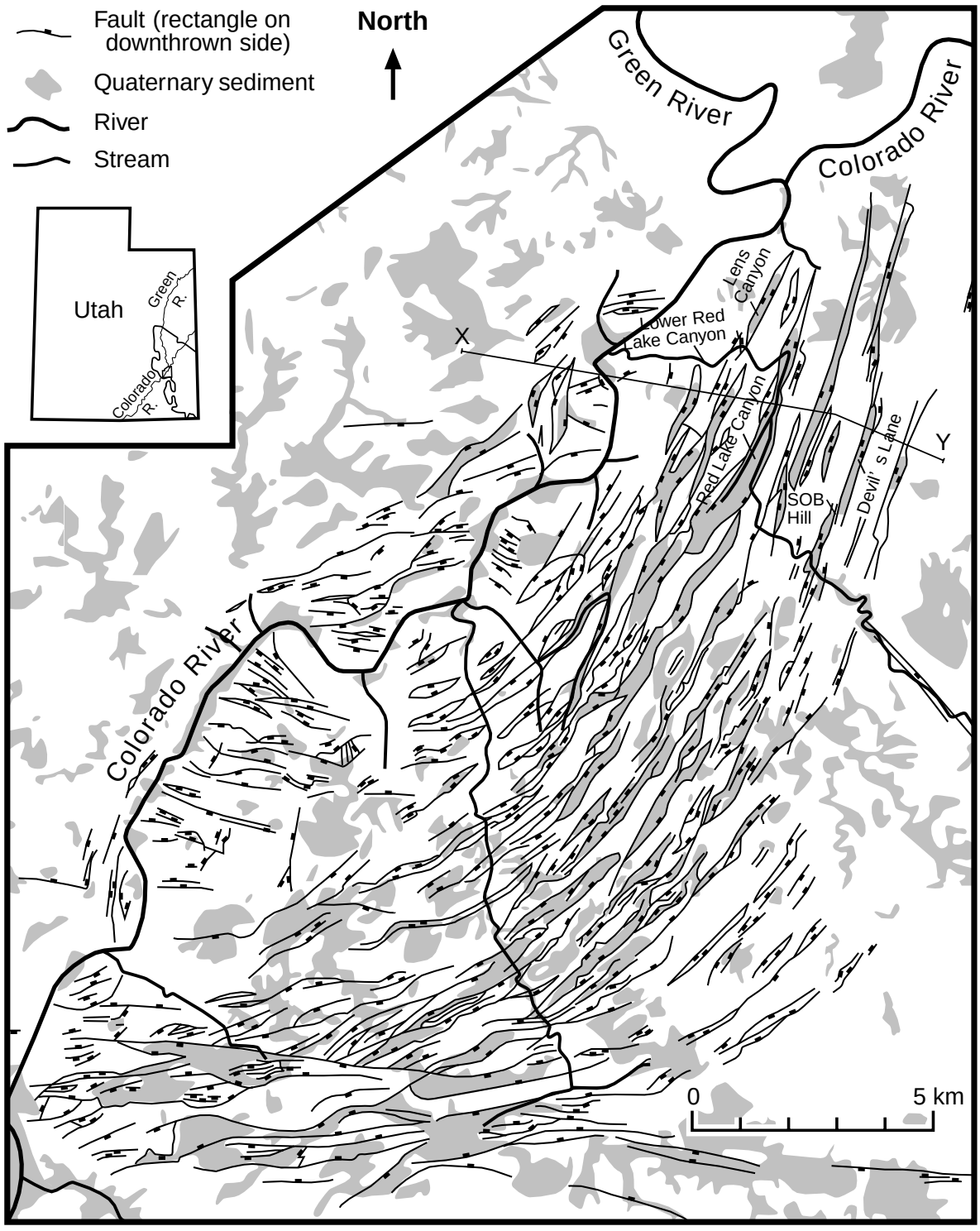

Fig. 1. Map view of fault traces and drainage system in The Grabens area of Canyonlands National Park, Utah (after Huntoon et al., 1982). Where not marked between closely spaced fault pairs, the downthrown side is always between the faults (i.e. grabens). Quaternary fill highlights the location of grabens. Line X–Y shows the location of cross-section in Fig. 2. The map of Utah in the top left shows the location of the fault-map boundary at the confluence of the Green and Colorado Rivers and the extent of the halite facies in the Paradox Basin (after Condon, 1997).

with strain weakening and tension limit characterized the sedimentary overburden. This rheology is the most appropriate one for numerically modeling faulting (Gerbault et al., 1998).

2. General geology of The Grabens

Comprehensive descriptions of the geology of the area appear in McGill and Stromquist (1979) and Woodward–Clyde

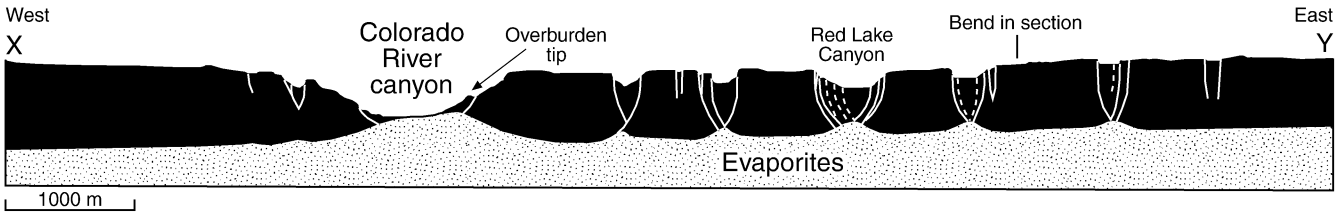

Fig. 2. Cross section across the northern grabens along the line shown in Fig. 1. Surface topography taken from 1:24,000 topographic maps. Surface geology from Huntoon et al. (1982) and Stromquist (1976). Geometry at depth and dashed faults are inferred from exposures in cross-cutting canyons, model results by us and others, salt structures elsewhere, and Moore and Schultz (1999). As in the finite element models illustrated here, additional minor faulting related to reactive diapir uplift is likely at the base of the overburden. Thicknesses of salt and overburden based on Woodward–Clyde Consultants (1983). No vertical exaggeration.

Consultants (1982, 1983) and references therein. Relevant details will be summarized here.

2.1. Stratigraphy

The lowermost unit involved in the deformation of the grabens is the Paradox Formation, which comprises cyclic evaporites, black shales, and carbonates (Hite, 1960, 1968; Baars et al., 1967). At Gibson Dome, about 20 km east of The Grabens, the Paradox Formation is 68% halite and about one-tenth as much anhydrite (Woodward–Clyde Consultants, 1982). The remainder is carbonate, siltstone, and shale. The Grabens are located near the southwest pinch-out of the halite facies (Fig. 1), so its thicknesses most likely varies considerably beneath the area of extending overburden.

The sedimentary section above the Paradox Formation comprises the Pennsylvanian Honaker Trail Formation, the Pennsylvanian–Permian lower Cutler beds, and the Permian Cedar Mesa Sandstone (Condon, 1997). Only the Cedar Mesa Sandstone is exposed throughout The Grabens area; the underlying formations crop out in deep canyons and locally near the base of graben footwall exposures. The nomenclature of the lower Cutler beds and upper Honaker Trail Formation has been hotly debated, but a useful resolution has recently appeared in a comprehensive discussion (Condon, 1997). The lower Cutler beds were previously assigned to the Rico Formation (Lewis and Campbell, 1965; Stromquist, 1976) or the Elephant Canyon Formation (Baars, 1962). As defined by Condon (1997), the base of the lower Cutler beds occurs at a color change that corresponds to the base of the Elephant Canyon Formation as it is commonly used (Huntoon et al., 1982, as discussed in Condon, 1997; Woodward–Clyde Consultants, 1982) and the base of the Rico Formation (Lewis and Campbell, 1965; Stromquist, 1976). Baars (1962) originally defined the base of the Elephant Canyon Formation some 125 m lower in the section.

The Honaker Trail Formation consists of interbedded limestone and sandstone in nearly equal amounts and a small percentage of shale (Condon, 1997). This formation is generally unfractured in drill core (Woodward–Clyde Consultants, 1982).

The lower Cutler beds comprise sandstone and arkose, minor conglomerate, mudstone, siltstone, and limestone (Condon, 1997). The limestone beds are most abundant near the top and base of the interval. The top of the uppermost limestone marks the top contact, corresponding to the top of the Rico Formation as used by Stromquist (1976). The thickness of the sedimentary section up to this level is 420–470 m (Woodward–Clyde Consultants, 1982, 1983). The overlying fluvial–eolian Cedar Mesa Sandstone (Langford and Chan, 1989; Condon 1997) of the Cutler Group crops out over most of the area, reaching a maximum thickness of about 60 m. The Cedar Mesa Sandstone is almost entirely sandstone, containing a few thin interbeds of siltstone. Joints in the Cedar Mesa Sandstone are exceptionally prominent in the northern portion of The Grabens, moderately developed in the southern portion, and inconspicuous in the middle portion. The representative thickness of the post-Paradox overburden used for our modeling was 450 m. This thickness represents a minimum value from the references just cited but matches estimates from specific studies of The Grabens (McGill and Stromquist, 1979; Ely, 1987; Schultz and Moore, 1996; Moore and Schultz, 1999).

2.2. Structural geology

Our representative cross-section through the northern portion of The Grabens (Fig. 2) shows layers of sedimentary rock dipping gently northwest above evaporites. This section appears similar to that of Moore and Schultz (1999, fig. 13), but differs in many key aspects. Some of these differences are: (1) the location and orientation of the section are shown (Fig. 1); (2) faults are vertical in the uppermost 100 m of the overburden, as observed in the field (McGill and Stromquist, 1974, 1979; Stromquist, 1976; Trudgill and Cartwright, 1994; Schultz and Moore, 1996; Moore and Schultz, 1999); (3) faults are distinguished between those observed, as shown on the Huntoon et al. (1982) map (solid lines), and those inferred (dashed lines); (4) the base of salt is placed accurately from an isopach map (Woodward–Clyde Consultants, 1983); (5) the west side of the canyon is shown, where faults extend the overburden in the regionally updip direction; and (6) multiple faults and

their downward projections are drawn to reflect our modeling results and those from physical models (see Section 5.2).

The most comprehensive reports on the deformation in The Grabens appeared in the 1970s (McGill and Stromquist, 1974, 1975, 1979; Stromquist, 1976). These studies describe the major features and analyze the mechanics and kinematics of the deformation. The Colorado River has eroded most or all of the sedimentary overburden down to the Pennsylvannian evaporites, exposing the evaporites as isolated diapirs in the north and continuous layers in the south. The studies concluded that erosion of the canyon removed the downdip confinement and allowed gravity-driven extension of the overburden. Judging from the down-cutting rate of the river, the deformation is estimated to have begun in the last 1.4 Ma (Biggar, 1987) to 0.5 Ma (McGill and Stromquist, 1974). The oldest deposits found as fill in a graben are dated at 65 ka (Biggar, 1987; Biggar and Adams, 1987). Because deposition requires some preceding graben growth, those deposits suggest a minimum age for the onset of deformation of 85 ka (Biggar, 1987). Numerous features indicate that the deformation is recent and ongoing, such as fissures, sinkholes, disrupted drainages, toppled blocks, and the Cataract Canyon rapids (McGill and Stromquist, 1974; Biggar, 1987).

No data constrain whether the grabens formed simultaneously or sequentially. From the general progression of increasing size and complexity toward the canyon, the onset of faulting has been interpreted to have migrated upslope from the canyon (Stromquist, 1976). The pattern of disturbed and abandoned drainages supports this conclusion (Biggar, 1987).

Erosional unloading by the Colorado River and its major tributaries induced the Paradox Formation to flow toward the low-pressure area beneath the canyons. This flow has created local anticlinal uplifts that follow the course of the canyons (Potter and McGill, 1978; Huntoon, 1982). The overburden east of the Colorado River canyon locally rotates and reverses the regional westward dip on the flanks of the anticline. Dips steepen to as much as 50° near the base of the canyon, although dips of 20° are more typical (Huntoon et al., 1982). Diapiric stocks emerge from the canyon floor in the northern part of The Grabens area, whereas progressively deeper erosion to the south exposes uplifted concordant salt.

Recent structural geology reports have detailed the displacement distributions along faults, fault interactions, and geometry of fault tips (Trudgill and Cartwright, 1994; Cartwright et al., 1995, 1996; Cartwright and Mansfield, 1998; Schultz and Moore, 1996). These papers have greatly advanced our understanding of faulting in Canyonlands. Because they mainly focus on laterally varying properties of the faults, however, they are less relevant to our study that simulates and analyzes fault patterns in two-dimensional depth sections.

3. Modeling method and parameters

Results of our numerical modeling strongly depend on several rock properties and model dimensions. Because most of these parameters are relatively well known for The Grabens system, the poorly known parameters are constrained to the limited range for which simulations produce realistic results. Therefore, the modeling not only reveals processes in the mechanical evolution of the Grabens, but also constrains probable values for the properties controlling that evolution. This section describes the numerical method used and the range of properties chosen for the simulations.

3.1. Finite element method

Realistic modeling requires a numerical method capable of capturing the response of the various rock types throughout their deformation history. Modeling salt tectonics presents a daunting challenge to most existing software packages. First, geologic deformations commonly progress to large finite strains, which greatly exceed those typically encountered in engineering problems. Second, the last decade has shown that most salt-related deformation in the shallow crust is best modeled using an overburden analog of brittle sedimentary rock, rather than the fluid overburden traditionally assumed (see review by Jackson (1995), and references therein). Realistic simulation of sedimentary rock deformation requires elasticity, normal-stress-dependent friction, strain weakening, and low tensile strength. Third, because erosion or deposition commonly accompanies extension, the numerical method should allow removal or addition of material during deformation. The modeling described here meets those three criteria (see Appendix A).

3.2. Rock properties

Several of the rock properties were varied systematically to determine their effect on structural evolution. The models we use to illustrate the mechanics of graben formation used the properties found that best simulate the grabens in Canyonlands. These properties correspond to properties reported in the literature. The effects of variations will be discussed in a later section.

3.2.1. Salt layer

The modeling was designed to capture the mechanical behavior of the Paradox Formation, which comprises mostly halite interbedded with minor cyclic anhydrite, black shale, and limestone and dolomite. Thus, we chose an average density of 2200 kg m^{-3}, which is slightly higher than for pure halite, to account for the denser minor components. Similarly, to simulate the Paradox Formation, a material law for halite should be strengthened slightly to reflect the impurities. Because we were interested in long-term steady-state behavior, we neglected the transient complexities

observed for halite during geologically short times and small deformations (e.g. Munson and DeVries, 1991; Aubertin et al., 1994). Over longer times, typical moderate- to fine-grained rock salt deforms as a Newtonian fluid that has no yield strength (Senseny et al., 1992; van Keken et al., 1993; Weijermars et al., 1993). Average strain rate for salt beneath the Grabens ranges between $10^{-13}\,s^{-1}$ and $10^{-14}\,s^{-1}$ (Moore and Schultz, 1999). Presumably, somewhat higher strain rates occurred locally because of discontinuous deformation of the overburden and expulsion of salt into the canyon. For these conditions and typical damp rock salt of moderate grain size, an effective viscosity in the range of 10^{17}–10^{18} Pa s is expected (van Keken et al., 1993). We chose the upper end of this range to account for the nonhalite components in the Paradox Formation.

Salt also behaves elastically, as shown by its seismic response and laboratory relaxation tests (Senseny et al., 1992). Thus, a viscoelastic (Maxwell) material law was used for the modeling (see Appendix A). As implemented in the numerical code, this behavior is characterized by a bulk modulus, a long-term shear modulus, an instantaneous shear modulus, and a relaxation time. The product of the last two values determines the viscosity. The elastic bulk modulus was set to 30 GPa, which is close to the 34 GPa measured for salt from the Paradox Formation just east of The Grabens (Pfeifle et al., 1983) and the 33 GPa average values in Senseny et al. (1992, Table 1) and Turcotte and Schubert (1982, Appendix 2, Table E). Lack of a threshold yield stress (Senseny et al., 1992) indicates a zero long-term shear modulus. The instantaneous shear modulus and relaxation time needed to be chosen such that their product would give the desired viscosity of 10^{18} Pa s. Measures of the shear modulus for halite range from 11 GPa (Pfeifle et al., 1983; Senseny et al., 1992) to 30 GPa (Turcotte and Schubert, 1982). Laboratory tests on rock salt indicate relaxation times of 24–36 h (Senseny et al., 1992). Unfortunately, these values yield a viscosity of about 10^{15} Pa s — far too low for natural salt behavior. Such a short relaxation time also leads to instability in the model calculations. Alternatively, if the van Keken et al. (1993) viscosity of 10^{18} Pa s and a shear modulus of 11 GPa are assumed, the calculated relaxation time would be 2.9 years. We have found no published values for rock-salt relaxation times over geologically significant durations. An estimate of relaxation time for asthenosphere rocks is 36 years (Turcotte and Schubert, 1982). Kenner and Segall (1999) used relaxation times of 5 and 58 years for lower crust and upper mantle having viscosities of 5×10^{18} Pa s and 9.5×10^{19} Pa s, respectively. Because the natural deformation we simulated occurred over some 100,000 years, the salt flow should not be sensitive to variations in relaxation time on the order of years. By decreasing the shear modulus about an order of magnitude to 1.4 GPa, a viscosity of 10^{18} Pa s gives a relaxation time of 23 years. These values are a good compromise between published values and numerical stability so were used for the salt analog in all of the runs.

3.2.2. Overburden layer

Abundant faults and joints indicate that the overburden deforms by the brittle behavior typical of shallow crustal rocks. When stress is progressively applied nonuniformly at relatively low temperatures and confining pressures, a rock typically strains elastically initially, then fails along discontinuities. With further deformation, the discontinuities evolve into faults sliding at steady state to give the rock a residual frictional strength. Therefore, a realistic simulation of brittle rock deformation requires elastic moduli, failure criteria for initial frictional yield, and criteria for strain weakening to the steady-state strength. The most widely used failure law in geology is the Mohr–Coulomb criterion (also termed the Navier–Coulomb criterion), which can be specified by a friction coefficient and cohesion value. For numerical convenience, the closely related Drucker–Prager yield criterion was used in the modeling (see Appendix A). For clarity, the Mohr–Coulomb equivalents of the Drucker–Prager parameters are described here, except for a limit on the tensile stress (see the end of this section). The plastic-flow law was non-associated, which meant that volume did not increase as the rock accumulated plastic strain. A non-associated constitutive model is the most appropriate for numerically simulating the initiation and growth of fault networks, because rocks do not increase in volume indefinitely as plastic strain accumulates (Gerbault et al., 1998).

Because the finite elements assume a continuum, plastic deformation results in localized, but continuous, failure (Rudnicki and Rice, 1975) rather than discontinuous fracturing or faulting. Softening accompanies plastic yield and shear band formation because of the non-associated flow law (Rudnicki and Rice, 1975; Rice, 1977; Needleman and Tvergaard, 1984; Cundall, 1989; Vermeer, 1990). The strain-weakening behavior we chose enhances the localization. This strain localization and softening effectively simulate faulting to large deformation in both nature and experiment (Barnichon and Charlier, 1996; Gerbault et al., 1998). Unlike most discontinuous numerical methods, the geometry and location of faults need not be specified. Instead, strongly localized shear and extension zones, analogous to faults and fractures, appear at stress concentrations and heterogeneities (Gerbault et al., 1998). Although the width of these zones depends on the element size (Bazant and Belytschko, 1987; Needleman, 1988; Sluys and de Borst, 1991), neither the geometry nor the qualitative behavior of the fault zones depends on mesh resolution (Pietruszczak and Mróz, 1981; Gerbault et al., 1998) (but also see Section 5.4 on *mesh effects*).

Although most rock properties were systematically varied, typical starting values needed to be chosen. For efficiency, single values were used that represented the bulk rock properties of the overburden. Given its mixture

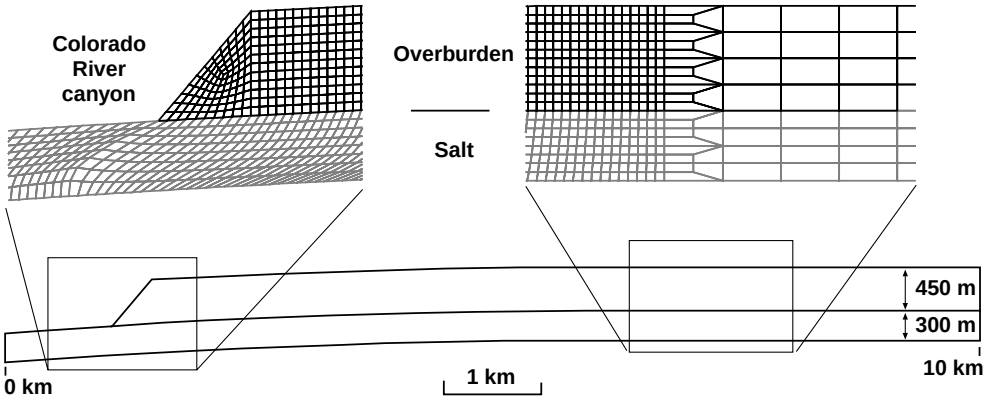

Fig. 3. Geometry of a typical model (that of Fig. 6) and the initial configuration of finite elements. Elements in the salt layer were constructed with the initially nonvertical boundaries shown so that angles in the elements sheared toward and then past right angles as the salt flowed toward the canyon. This configuration minimized the final angular distortion of the elements.

of sandstone, shale, and lesser limestone, the overburden was modeled by using an approximate mean value for all of those rock types, namely a Young's modulus of 25 GPa and a Poisson's ratio of 0.25 (Turcotte and Schubert, 1982, Appendix E). Friction coefficients for rocks depend on a large array of variables, but 0.6 is a reasonable and widely quoted value for these rock types (e.g. Marone, 1998). Cohesion values are more poorly known, but laboratory tests typically yield values ranging from 0.3 MPa for claystones to 36 MPa for a limestone (Handin, 1966). These values should be scaled down by about a factor of 10 to account for the size and character of the rock mass considered here (Pusch, 1995; Schultz, 1996). Our systematic modeling found that a value of 1 MPa was the best for reproducing the fault pattern in Canyonlands. This value falls within the expected range.

The most poorly known rock properties determine the evolution of the failure law as strain accumulates. Intact rock is stronger than fractured rock; in fact, localization of failure on discontinuities and narrow fault zones generally signifies strain weakening. Velocity, time, and distance effects on frictional strength have been described from laboratory tests (e.g. Marone, 1998), but extrapolation to larger rock masses is still conjectural. Because the faults in Canyonlands show displacements of less than about 100 m, very low friction typical of highly evolved plate boundary faults seems unwarranted. Therefore, we defined strain weakening as a moderate decrease in friction angle from the initial 31° to a residual 26°. During the same strain interval, cohesion decreases to zero. Weakening in the best models occurred over a range of equivalent plastic strain from 0.01 to 0.02 (see Appendix A).

A nonzero cohesion in the linear failure criterion used here implies a tensile strength for the rocks. Rocks are notoriously weak in tension, so a limit on allowable tensile stress was made part of the failure criterion. Because the Drucker–Prager criterion is expressed in terms of stress invariants, the tensile limit is actually specified as a minimum pressure limit, rather than the minimum (tensile) normal stress cutoff commonly used in a Mohr–Coulomb failure criterion (see Appendix A). We generally specified the minimum pressure, or pressure cutoff, to be half the cohesion. Therefore, the pressure cutoff in the most realistic models was −0.5 MPa.

3.3. Model geometry

The grabens in Canyonlands formed by gravity-driven extension toward the free boundary created by erosion of the Colorado River canyon. An example of the finite element mesh used to model this system appears in Fig. 3. Variations of the basic geometry included changes in slope and length of the model. All but two of the models started with the same overburden and salt thicknesses of 450 and 300 m, respectively. Test runs showed virtually equivalent results regardless of whether the simulated canyon cut through all or only 300 m of the overburden. However, decreasing the canyon depth to half or less of the overburden thickness effectively stops the gravity spreading because of the buttressing effects of the thick canyon floor. For simplicity, runs shown here used a canyon cutting through to the salt. Similarly, gradual rather than instantaneous excavation of the canyon had a negligible effect on the structural evolution. Some runs also included simulated open joints that were 100 m deep and spaced 100 m apart along the top surface. These joints were element surfaces that could freely separate (or numerically overlap), but their presence produced no significant difference in the results.

For most of the runs shown, emergent salt was periodically eroded as it flowed into the canyon. Generally we removed a layer of salt elements when the salt surface rose about 150 m above its original elevation. The precise timing of that erosion slightly affected the extension rate, but it had a negligible effect on the structural pattern and growth sequence. Plots of gliding rate in the overburden showed only minor jumps at these periodic removals of approximately 70 m of salt (see Section 6.3).

Most of the results displayed in the figures show contours

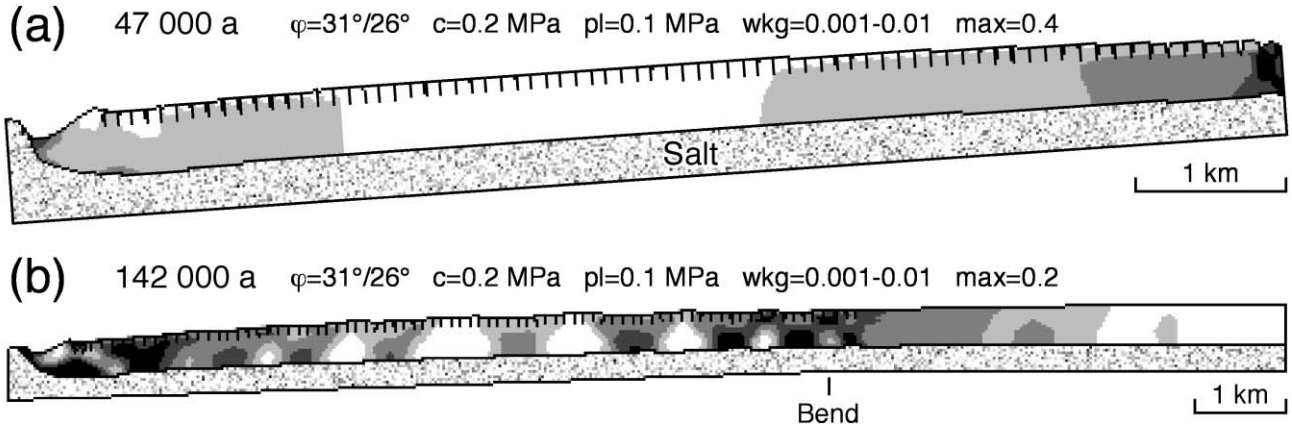

Fig. 4. Finite element models, in which the overburden slope was constant: (a) at 4° over the entire model, or (b) at 2° below a sharp bend (hinge line). In both models, faulting concentrated at the top of the slope and at the toe of the overburden. These models had free surfaces (no contact) simulating vertical joints, which extended 50 m down from the top. The joints had negligible influence on the fault geometries and locations. Gray shades show contours of equivalent plastic strain from low (white) to high (black). These shades are used here to display the joints clearly, but are reversed in the following figures. Values above the models record the following: a = duration of model in years; φ = friction angle, for both initial/weakened; c = cohesion; pl = negative pressure limit (similar to a tensile stress limit); wkg = range of strain from onset to fully weakened; and max = maximum contour level. The minimum contour level is always 7% of the maximum. White fills areas less than the minimum and black fills areas more than the maximum.

of equivalent plastic strain. Localized strain is the equivalent of a fault (for a shear zone) or joint (pure extension). The width of the zone is generally a function of the element size. Decreasing the element size decreases the width of the fault zone and increases the resolution of the deformation.

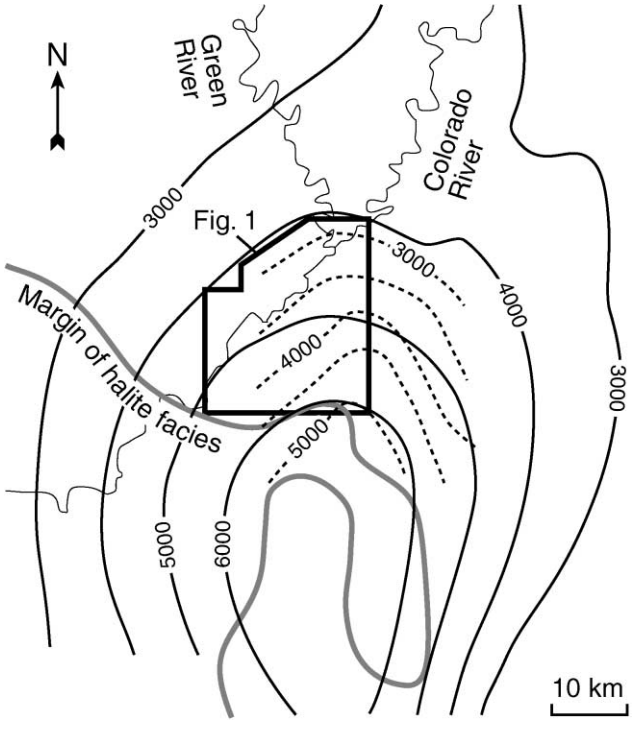

Fig. 5. Structure contours (in feet) for the base of the Cutler Group (solid lines, from Condon, 1997) and the top of the Paradox Formation (dashed lines, from McCleary and Romie, 1986). The gray line marks the southwestward pinch-out of halite facies in the Paradox Formation (from Condon, 1997), and the black box shows the location of Fig. 1 and the general limit of graben faulting. Dip of bedding is perpendicular to structure contours, so northward along the canyon in The Grabens area the dip swings from normal to parallel to the general canyon trend.

4. Model results — major features

4.1. Slope effects

The simplest model had a constant slope of 4°, which is the average slope quoted by previous authors (McGill and Stromquist, 1979; Trudgill and Cartwright, 1994; Schultz and Moore, 1996; Moore and Schultz, 1999). As shown by contours of equivalent plastic strain (Fig. 4a), the modeled overburden simply glided downslope as a coherent block slightly upturned at its toe. All extension concentrated at the upslope boundary. This response clearly did not resemble the progressive upslope failure inferred for the natural grabens of Canyonlands. In addition, the gliding was unnaturally rapid, even though no salt was eroded from the canyon floor. These unrealistic features all result from an excessively steep slope.

The models described here were intended to simulate the grabens in the northern portion of the system. The surface is at approximately the same stratigraphic level across the grabens, so surface slope mimics stratigraphic dip. We measured a surface slope of 2° or less on several profiles that connected photographically correlative layers across the grabens, similar to an average dip of 1.4° measured from structure contours on formations of the Cutler Group (Fig. 5; McCleary and Romie, 1986; Condon, 1997) and dips on unfaulted rocks surrounding the grabens (Huntoon et al., 1982). Similarly, structural contours on the top of the Paradox evaporites indicate a dip of 2.5° (Elston and Shoemaker, 1961) or 1.6° (McCleary and Romie, 1986) across The Grabens.

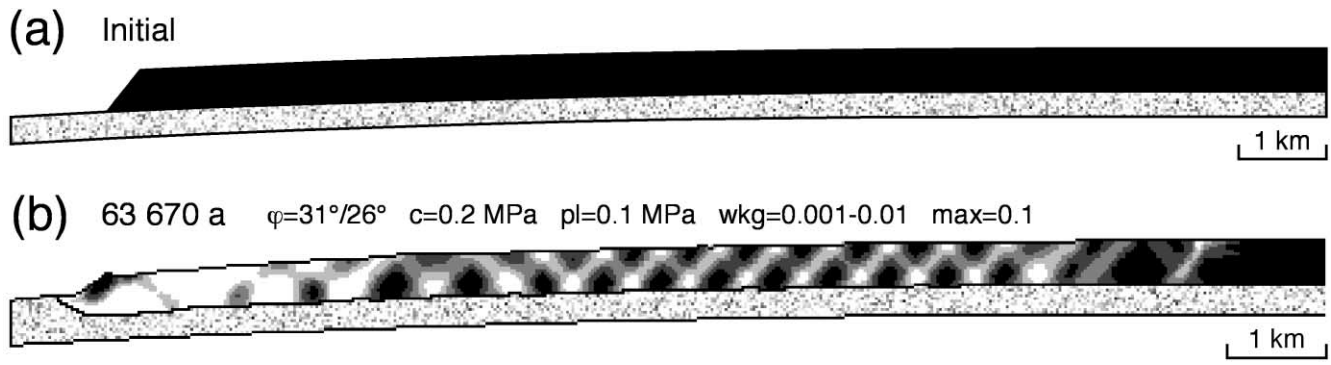

Fig. 6. (a) Initial and (b) deformed states of a model in which the slope increases progressively toward the canyon. The deformed state shows only the left 13 km of the 15-km-model; the remainder has no strain. Contours of plastic strain range from low (black) to high (white) in the overburden (the gray gradations are reversed from those in Fig. 4 in this and following figures). Model had the same material properties as that in Fig. 4.

Therefore, we built a model that had a slope of only 2° and was lengthened horizontally to the right (Fig. 4b). In the overburden, faulting was distributed as spaced grabens, but most of it was concentrated near the slope break and the rotated toe. Faulting tended to propagate upslope from the toe and downslope from the slope break. The later stages of the model indicated that nearly all of the extension was accumulating at the top of the slope.

Preferential extension at the top of the slope carries implications for the relative movement rates of salt and overburden — that is, the fundamental question of whether salt flow drives or resists glide of the overburden. Extensional failure in the overburden marks the location where stress first exceeded the yield strength. Vertical stress was relatively constant laterally in the layer because it derived simply from gravity acting on a uniform thickness. Given this laterally homogenous maximum stress, the location having the least compressive stress at a certain depth would be most likely to fail first. Therefore, the modeled overburden at the top of the slope had less horizontal stress than at the base of the slope. In effect, the overburden stretched at the upslope end and piled up downslope, except at the toe of the block, where rotation, the canyon face, and salt flow to the free surface created local complications. If, instead, canyonward salt flow drove the extension, the flow rate would have been maximum at the toe of the overburden and faulting would appear there first. The concentrated extension at the top of the slope indicates that the salt flowed slower than the overburden and resisted its downslope glide. Further evidence of these relations will be discussed in Section 6.2.

In the Canyonlands grabens, progressive upslope failure is inferred to have begun at the toe of the overburden, which requires the opposite gradient in horizontal stress from these models. We explored several changes to the models to replicate the geological upslope progression of faulting. An obvious change is to alter the surface gradient so as to decrease the horizontal compressional stress toward the

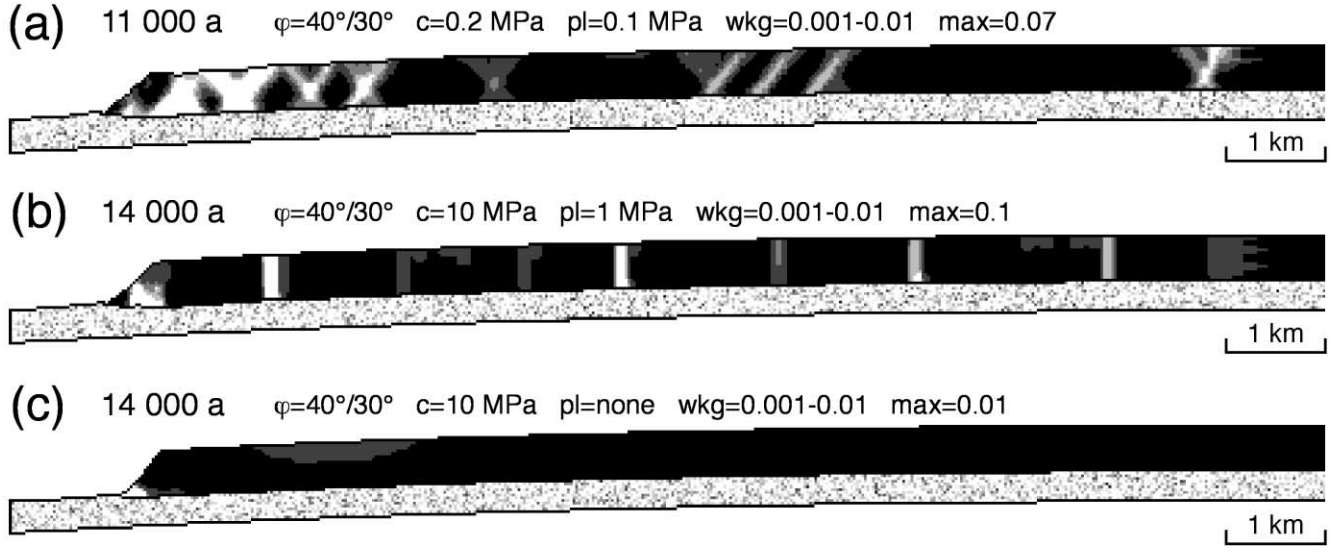

Fig. 7. Models having increased friction angles and varied cohesions. (a) Same model as Fig. 6 but with increased friction angles. (b) Same model as (a) but with cohesion and pressure limit increased. (c) Same model as (b) but with no negative pressure limit.

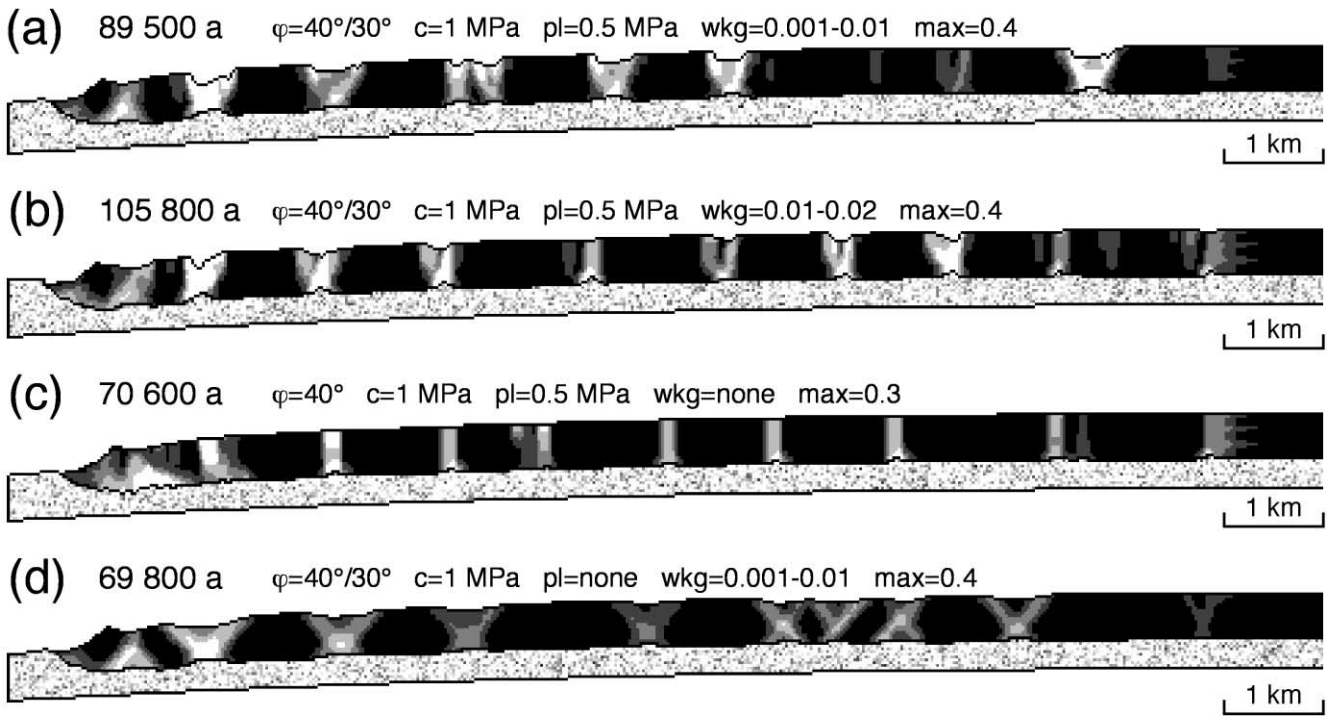

Fig. 8. Models having large friction angles, moderate cohesion, and varied weakening. (a) Same model as Fig. 7a but with cohesion and pressure limit decreased. (b) Same model as (a) but with the onset of weakening delayed and prolonged. (c) Same model as (a) but with no strain weakening. (d) Same model as (a) but with no negative pressure limit.

toe of the overburden and encourage extension there. In addition, there is no evidence in nature for faulting at a stress concentration induced by a hypothetical sharp hinge at the top of the slope. Accordingly, the models in Fig. 6 had a slope that increased progressively from horizontal at the eastern boundary (right side of model) to almost 3° at the toe. The slope was a section of an ellipse. This slope change increased the gliding tendency toward the toe, which counteracted the viscous basal drag from salt. In plate tectonics, this change would be analogous to changing the driving force of plate movement from ridge push to slab pull.

Fig. 6b shows the deformed model having the same material properties as the models in Fig. 4. The smoothly increasing slope substantially altered the faulting pattern. A continuous succession of grabens formed in the sloping part of the overburden. Most of the grabens were symmetrical, although those in the upper part of the slope developed larger strains on the canyonward-dipping faults. Extension was greatest in the few kilometers nearest the toe. Therefore, the propagation of faults more closely matched the natural grabens, but their shape and spacing did not. The natural grabens (Fig. 2) are narrower, are bounded by steeper faults, and are separated by undeformed blocks.

A progressively increasing slope is not the only geometry that forms faults sequentially away from the free face of the overburden. As shown in Section 6.3, models that are horizontal or that slope away from the canyon also display that progression of faulting. However, the increasing slope model more closely resembles the natural slope, so that model was used to systematically vary the material properties to create more realistic fault patterns.

4.2. Variations in rock properties

Because material properties can have a strong effect on fault dip and spacing, the following models varied the overburden properties to better match the geological pattern in Canyonlands. The model in Fig. 7a increased the friction coefficient to 0.84 (40° friction angle) in our expectation of steeper faults. This friction angle also matches experimental measurements at pressures typical of upper crustal rocks (Byerlee, 1978). The downslope faults were slightly steeper, but the dominant effect was a decrease in the number of faults and a clustering of them in widely spaced groups. The tendency toward asymmetric graben development in the upper part of the slope was more apparent. The large areas of undeformed overburden indicate that the increased friction angle had much more effect on strength than on fault orientation. However, a 50-fold increase in cohesion to typical laboratory values for sedimentary rocks (Handin, 1966) resulted in vertical faults (Fig. 7b). These faults developed singly and segmented the overburden into undeformed blocks between 1 and 1.5 km wide. These faults accommodated extension by opening rather than by shear, resembling tension fractures or joints. The model in Fig. 7c used the same high friction angle and cohesion but removed the tension cutoff. The result was an overburden too strong

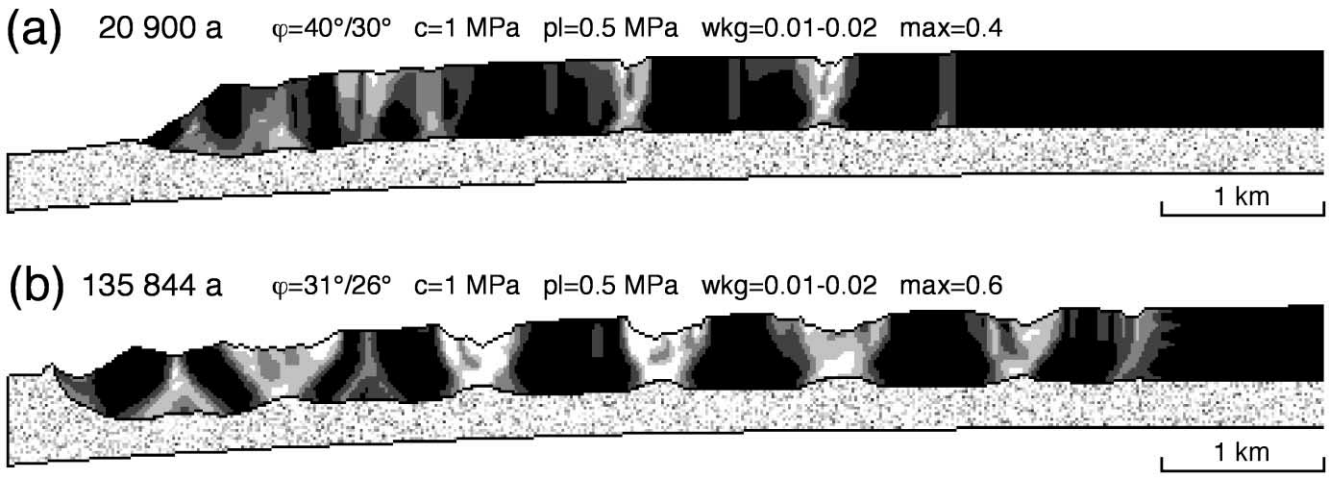

Fig. 9. Shorter models. The complete models were 10 km wide, but only the left 8 km is shown. (a) Model with the same material properties as that in Fig. 8b. (b) Model with decreased friction angle.

to fail at all in a reasonable time period under the simple gravitational loading (longer times might allow sufficient salt flow to induce local flexural failure). Thus, simulations using rock properties based on laboratory measurements of small, unfractured test specimens do not produce fault patterns characteristic of the rocks in Canyonlands. A tension limit is necessary, and friction and cohesion values need to be reduced, as suggested by Schultz (1996) for large, jointed masses of sedimentary rock.

Since cohesion variation caused the greatest change in fault orientation in the preceding models, the models in Fig. 8 used an intermediate value of cohesion (1 MPa and tension limit of −0.5 MPa) in an attempt to produce faults intermediate between vertical and moderate dips. The model in Fig. 8a shows results of the same model as that of Fig. 7b, but with this lower cohesion. The simulated grabens had fault dips and intergraben spacing similar to those of the natural ones. The dip on the faults reflects a combination of tensional opening and shear failure; that is, the Mohr circle intersects the tensile-limit part of the failure envelope in the shallow overburden but intersects the frictional part in the deeper overburden. A more realistic hyperbolic or exponential failure envelope that smoothes the transition from tensional to frictional behavior would presumably result in faults curving smoothly away from vertical in the near surface. The progression of faulting and duration of gliding resembles what happens in the geological example. However, some of the grabens were too wide. Delaying and prolonging strain weakening (Fig. 8b) steepened the faults more and narrowed the grabens. To further illustrate the strain-weakening effect, we ran another model (Fig. 8c) that had no weakening. Single vertical faults resulted. Therefore, the weakening interval in Fig. 8b seems appropriate. The same properties as those in Fig. 8a but no tension limit (Fig. 8d) created even wider grabens having no fault steepening near the surface.

This series of models shows that the faulting pattern depends sensitively on several material properties, especially cohesion and strain weakening. Unfortunately, the actual weakening behavior in natural rocks is poorly known. Experimental results are suspect because of their dependence on experimental apparatus and samples that are typically unfractured, small, and homogeneous. In subsequent models of the grabens, we used the slower weakening interval and moderate cohesion of the model in Fig. 8b because those properties produced fault patterns that most closely resembled the natural grabens.

The preceding models had an overburden sheet substantially longer than that in the northern portion of the Canyonlands grabens. Thus, Fig. 9a shows a shorter model that used the best properties found for the preceding models and the same type of progressively increasing slope. The faults were too steep and too widely spaced, when compared with the natural ones. The model in Fig. 9b used a decreased friction coefficient, the more commonly quoted value of 0.6 (friction angle of 31°), which led to a better result. This model compares favorably to the geologic cross-section at the same scale in Fig. 2, particularly considering the sensitivity of rock properties. The grabens in the model developed the appropriate width and spacing. For a reasonable salt viscosity of 10^{18} Pa s, their offset and the overall extension accumulated in an appropriate time span on the order of 100 ka. Particularly gratifying is the fact that the friction angles, cohesion, and tension cutoff are all close to typical values inferred in natural rocks at the kilometer scale. The most realistic model resulted from the most realistic values, and only the cohesion and weakening interval differed from that with which we started. The original choice of those anomalously low properties derives from the majority of our modeling work on weak, often poorly lithified sediments in the Gulf of Mexico.

Although the structural patterns in the models and in nature coincide, the resemblance does not prove that the same rock properties were responsible. Different properties

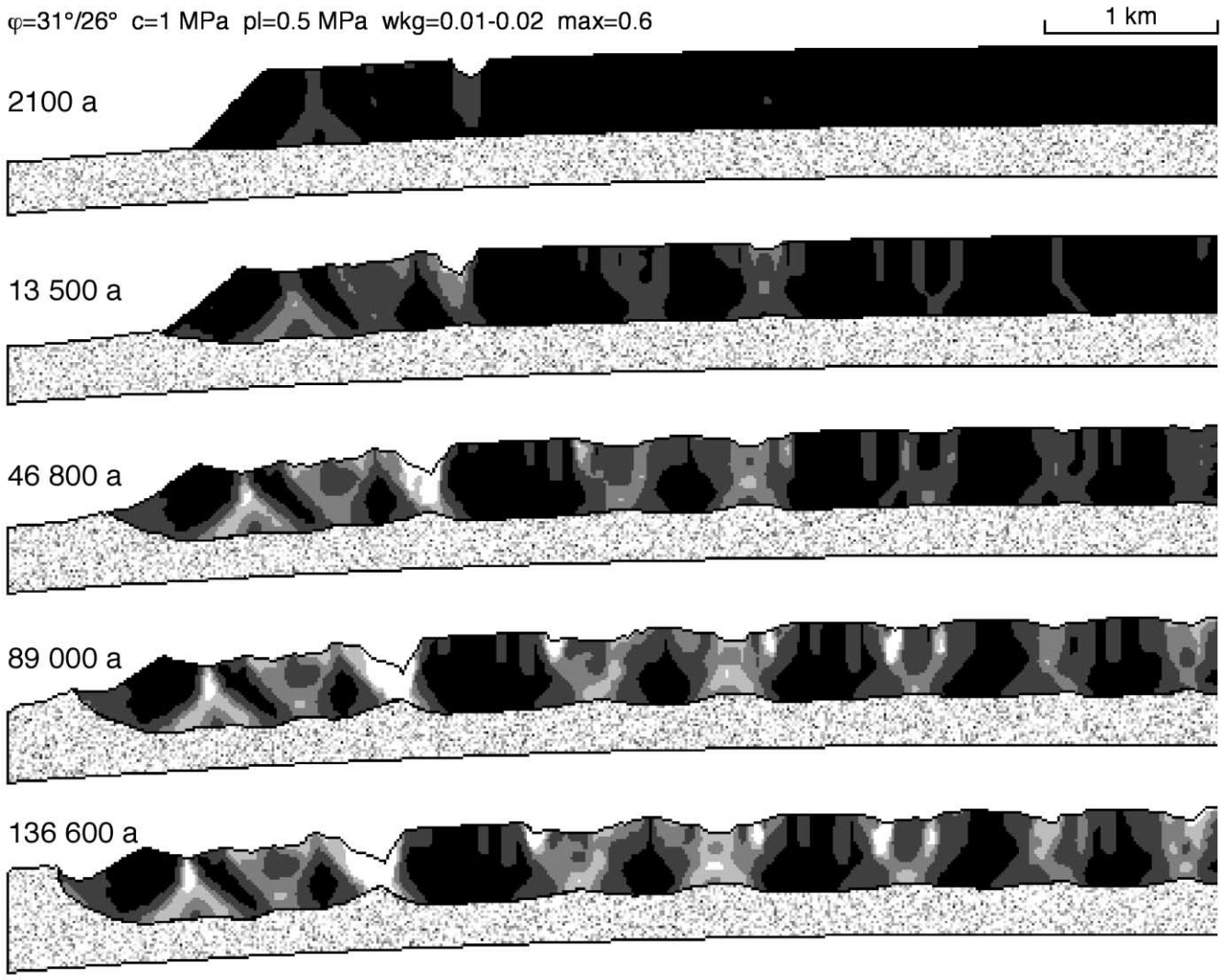

Fig. 10. Same model as in Fig. 9b but with a 100-m-deep notch added to the top surface initially. This notch represents the stream valley that appears to have predated graben formation and is now Red Lake Canyon (Fig. 1).

may have similar effects, such that a different combination of values could produce a similar structural outcome. However, the starting and ending configuration and properties of the Canyonlands grabens are unusually well known for geologic systems. The possible range of variables is therefore unusually small for a geological simulation. A combination of values in the numerical simulation that all fall close to the expected values of these rocks and that produce a similar structural pattern argues strongly for the validity of the values.

5. Model results — minor features

5.1. Preexisting topography

The generalized section in Fig. 2 represents the northern portion of The Grabens, just south of a major side canyon of the river (Lower Red Lake Canyon). On this cross-section, the widest and deepest graben is the third one upslope from the canyon, called Red Lake Canyon. In the models, however, that distinction belongs to the first graben. The pregraben land surface was not flat in The Grabens area; a clearly defined stream system (McGill and Stromquist, 1974; Biggar, 1987) coalesced and drained along the location of the present Red Lake Canyon graben on the cross-section and exited out the side canyon. Thus, a significant valley probably existed there when the extension began (Stromquist, 1976). Early growth of the Red Lake Canyon graben intercepted westward-flowing streams east of it before grabens there began to grow and disrupt drainages, resulting in the observed paucity of abandoned channels between the river and Red Lake Canyon (Biggar, 1987). The significant surface relief of the Red Lake Canyon stream valley may have controlled the initial location and early growth of the later large graben there.

This hypothesis is tested in the model shown in Fig. 10, which was identical to the one in Fig. 9b except for the

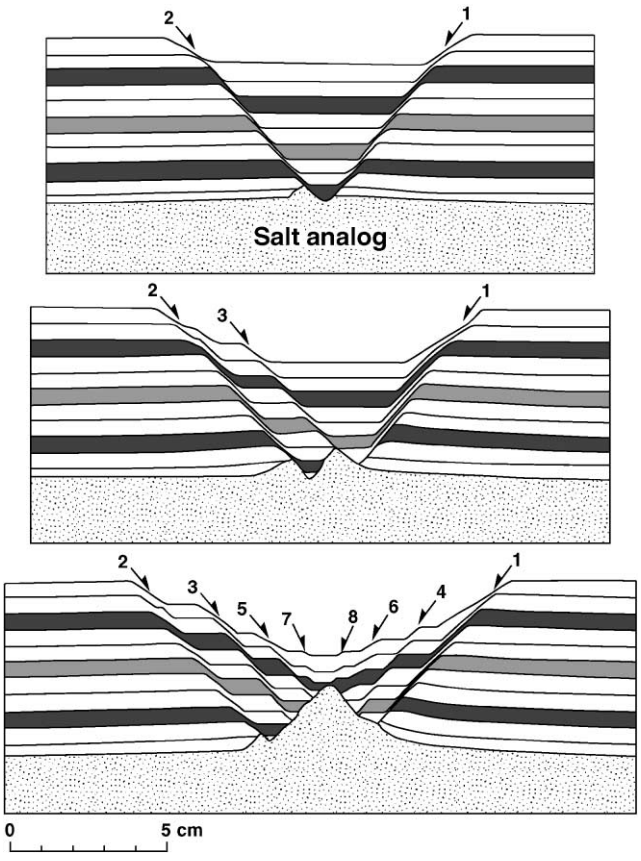

Fig. 11. Cross-sections showing growth of a reactive diapir underlying a graben (modified from Jackson and Vendeville, 1994). Cross-sections were cut at different times from three initially identical physical models. Silicone polymer (speckled, at base) simulates salt. Dry sand (white and gray layers) simulates sedimentary rock overburden. Faults are numbered in sequence of formation.

valley notch in the top surface. Because the valley not only created a thinner zone in the overburden but also acted as a stress concentrator, it strongly controlled the model evolution, as shown by the sequence of sections. The oldest graben formed below the valley, and it remained the largest. The faulting clearly progressed upslope in this model. For these reasons, addition of the likely prefaulting relief improved the model results to where they match the observed structures closely. The grabens also developed asymmetrically, showing a tendency to change upslope from a dominant west-dipping fault to a dominant east-dipping fault. This general trend was noted in the field by Moore and Schultz (1999), but their observed change in sense of asymmetry is located much closer to the Colorado River.

5.2. Minor structures

Although the grabens are the major structures in the deformed models, other minor structures are notable.

One of the controversies about the grabens in Canyonlands is the subsurface geometry of the faults. McGill and Stromquist (1975) showed several possibilities, distinguished by whether the graben-bounding faults were subvertical or converged to intersect at or above the salt contact. They argued strongly for convergence, on the basis of field observation and physical modeling. Although Trudgill and Cartwright (1994) showed the faults converging to intersect above the salt, later papers by the same authors (Cartwright et al., 1995, 1996) assert subvertical faults and pluglike graben blocks on the basis of observations in side canyons. Our personal observations in Lower Red Lake Canyon, Cross Canyon, and Y Canyon clearly show faults that converge at or above the level of the salt contact, as argued for by Moore and Schultz (1999) and McGill et al. (2000). The numerical models shown here support that geometry.

McGill and Stromquist (1975) speculated that the bottom point of the graben block was 'brecciated and faulted' to produce a flat bottom and that none of that rock 'escaped into' (projected into and was carried away by) the flowing salt. Although they recognized that ridges of ductile substratum rose beneath the grabens in their physical models owing to decreased overburden pressure, they did not describe the mechanism accommodating that upwelling. Our numerical models show similar upwellings of salt beneath each down-dropped graben block. Physical models and observations on salt structures elsewhere show these to be typical features in extensional salt tectonics that are known as reactive diapirs (Jackson et al., 1994), which were inferred to underlie the Canyonlands grabens by Moore and Schultz (1999) on that basis. These diapirs rise because of the weakening and unloading effect of the graben (Vendeville and Jackson, 1992). Rather than brecciation of the fault tip, reactive diapirs rise by progressive inward dissection of the graben block, which produces downstepping of the ground surface inward toward the center of the graben system above a rising salt contact (Fig. 11). The resolution of the finite element models is too coarse here to reveal that process plainly, but that tendency is clearly apparent (e.g. Figs. 9b and 10). These models predict that the bedrock surface beneath the alluvial fill in the Canyonlands grabens is not flat, as previously assumed implicitly (McGill and Stromquist, 1975) or explicitly (Cartwright and Mansfield, 1998), but deepens toward the center. Such a geometry would explain the seemingly contrary observations of a relatively shallow bedrock surface in sinkholes at the graben margins and geophysical indications of a much deeper bedrock surface at the graben center (Bush et al., 1996; Moore et al., 1997). The inward-stepping faults would form progressively as extension increased; thus, the exposed bedrock ramps where fault displacement dies out are expected to be relatively flat, as observed. However, fault slivers stepping downward toward the center of a graben that narrowed through time are observed at the south-dipping relay ramp of the Devil's Lane graben (Fig. 12) (Moore and Schultz, 1996) and elsewhere. The mechanics of reactive diapirism nicely

Fig. 12. View west across the northern end of the southern segment of the Devil's Lane graben, taken at the SOB Hill stepover (Fig. 1). The outcropping main portion of the south-dipping ramp is just off the photo to the right. Shown here are the west wall of the graben and two fault-bounded slivers that increase in dip toward the center of the graben and the deeper, buried ramp. White lines indicate dip of each sliver. Trees are approximately 2 m tall.

explain these features that "are not fully understood" (Moore and Schultz, 1996).

Rotation at the toe of the overburden slab complicates the pattern of simple extension noted elsewhere. Salt flow toward the free surface in the canyon causes rotation and uplift of the overburden tip, shear on the base of the overburden, and subsidence behind the tip where salt has been expelled. Uplift and rotation of the rocks in the canyon wall of the model simulate formation of the Meander Anticline centered on the Colorado River canyon (Potter and McGill, 1978; Huntoon, 1982). The subsidence and rotation also complicate formation of the first graben away from the canyon. This graben originates wider than the simple grabens upslope. Multiple faults within the graben create a pattern of subsidiary horsts and grabens within the larger graben (Figs. 9b and 10). This behavior may correspond to the small grabens closest to the river, which tend to be more irregular and discontinuous than the upslope grabens in Canyonlands (Fig. 1).

Another major feature due to rotation is the uplifted horst block that forms the first major structure upslope from the canyon in the models. Such a feature has not been described in Canyonlands. However, recent field observations in Lower Red Lake Canyon, a major side canyon, reveal a similar geologic structure in cross-section just west of the Lens Canyon graben (Fig. 13, locations in Fig. 1). Distinctive sedimentary layers, two of which are marked by solid and dashed lines, define the offsets across faults. The bounding faults of the triangular horst intersect below the ground surface on the skyline, and the west-dipping fault continues upward such that the left (riverward) block has been dropped. Similar relations are suggested in the models. Although the natural horst is located farther away from the main canyon wall in nature than in the model, the structural location between the rotated toe and the first major graben is the same. This horst did not accommodate lateral extension but, rather, upward rotation of the overburden tip as salt flowed into the canyon, as shown by slip on the faults that decreases upward in the models. Stretching of the sagging, concave-upward bottom of the overburden created the faults that bound the uplifted horst. Analogous to different types of grabens that originate from arching rather than lateral extension, this horst derived from subsidence over salt expelled into, and eroded from, the model canyon.

5.3. Slope variations

As previously mentioned, our measured average slope angles differ from those of previous authors. All agree, however, that the slope flattens westward within a couple of kilometers of the canyon. Part of this change is due to uplift of the Meander Anticline, but that effect is restricted

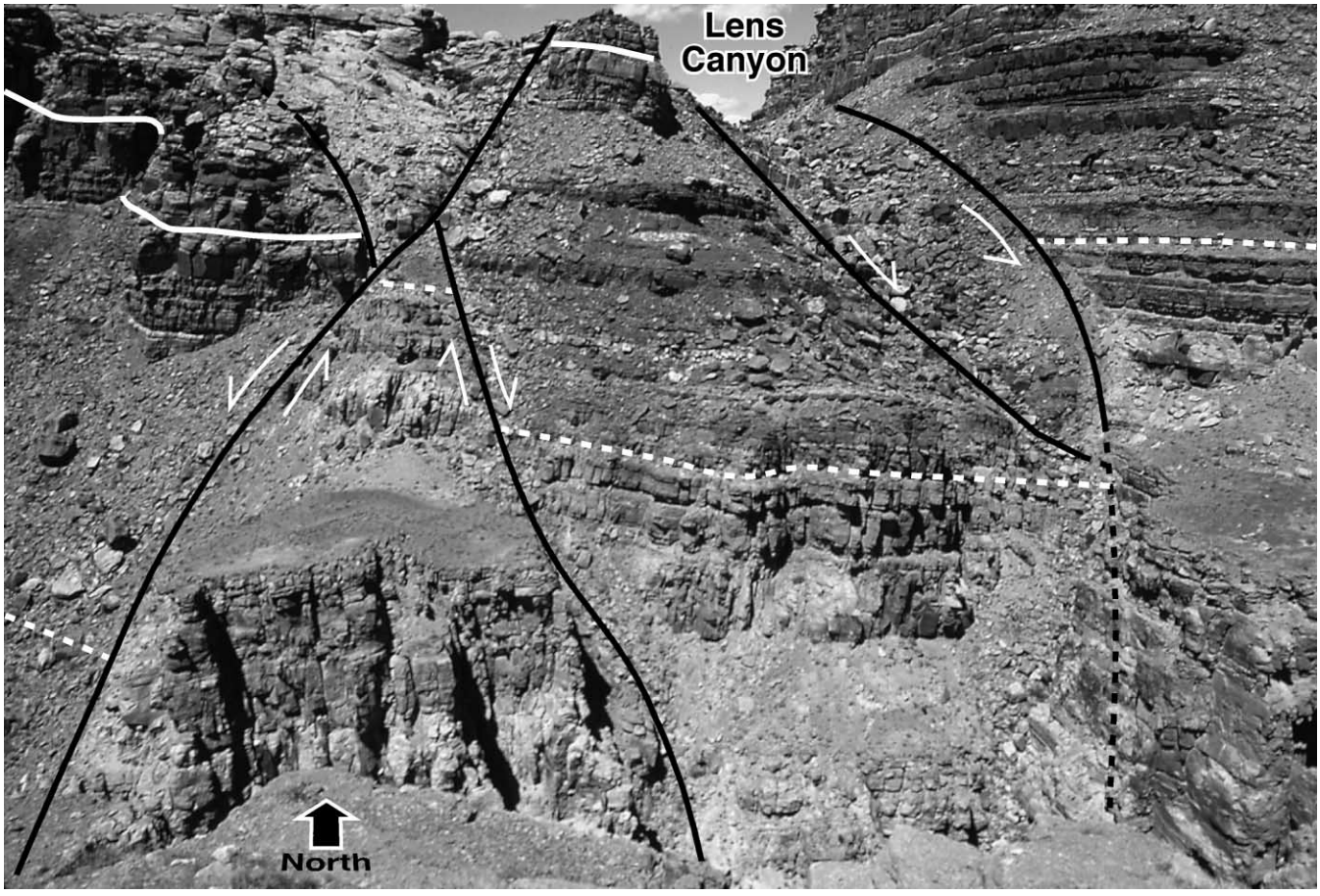

Fig. 13. Horst exposed in the north wall of Lower Red Lake Canyon, west of the Lens Canyon graben (see Fig. 1 for locations). Solid and dashed white lines mark distinctive horizons that can be correlated across the faults. A foreground ridge in the lower right hides the downward continuation of the east graben fault in the photo.

to a narrow strip along the canyon. Regardless, a decrease in slope toward the river is opposite to the increasing slope required in the preceding models to create upslope propagation of faulting. We constructed additional models to further explain the effect of surface slope. One set of models considered the end-member case of no slope or opposite slope, and others varied the shape of the slope to better replicate nature. All of these models used the optimal rock properties of the model in Figs. 9b and 10.

The model in Fig. 14a shows the results of no slope at all: that is, initially horizontal top and basal surfaces. Otherwise, the model dimensions and geometry are the same as in Fig. 9b. The no-slope model removed the driving force caused by a downslope component of gravity. The results resemble those for a progressively steepening slope — the grabens sequentially formed and grew rightward (eastward) from the free face at the canyon — but the extension rate was much slower. Spacing widened slightly between the grabens, so that only four grabens formed instead of the six in Fig. 9b. There, a progressively steepening slope caused rightward propagation of grabens because the steepest part of the model had the greatest downslope component of gravity and extended first. By comparison, grabens propagated rightward in the horizontal model because of a balance between viscous drag in the salt and gravity collapse of the overburden allowed by lateral extension toward the free face. The longer the block of overburden that translates, the greater the total viscous resistance from the salt. Therefore, the overburden near the free face has the least resistance to lateral translation and fails first. As that short block moves canyonward and separates from the rest of the overburden, the intervening graben forms a new low-pressure zone similar to that of the free face at the canyon. This zone allows the next block of overburden to the right to separate and begin moving leftward. Thus, for different reasons, a progressively steepening slope and no slope produced similar structures that resemble the grabens in Canyonlands.

A reversal of the slope also produced progressive faulting away from the canyon and realistic grabens (Fig. 14b). This reversal restricted graben growth to the area near the canyon, even after a far longer time span than that in the other models. This slope and the resulting structures resemble those of the area west of the Colorado River canyon, where only one or possibly two small grabens have formed (Fig. 1).

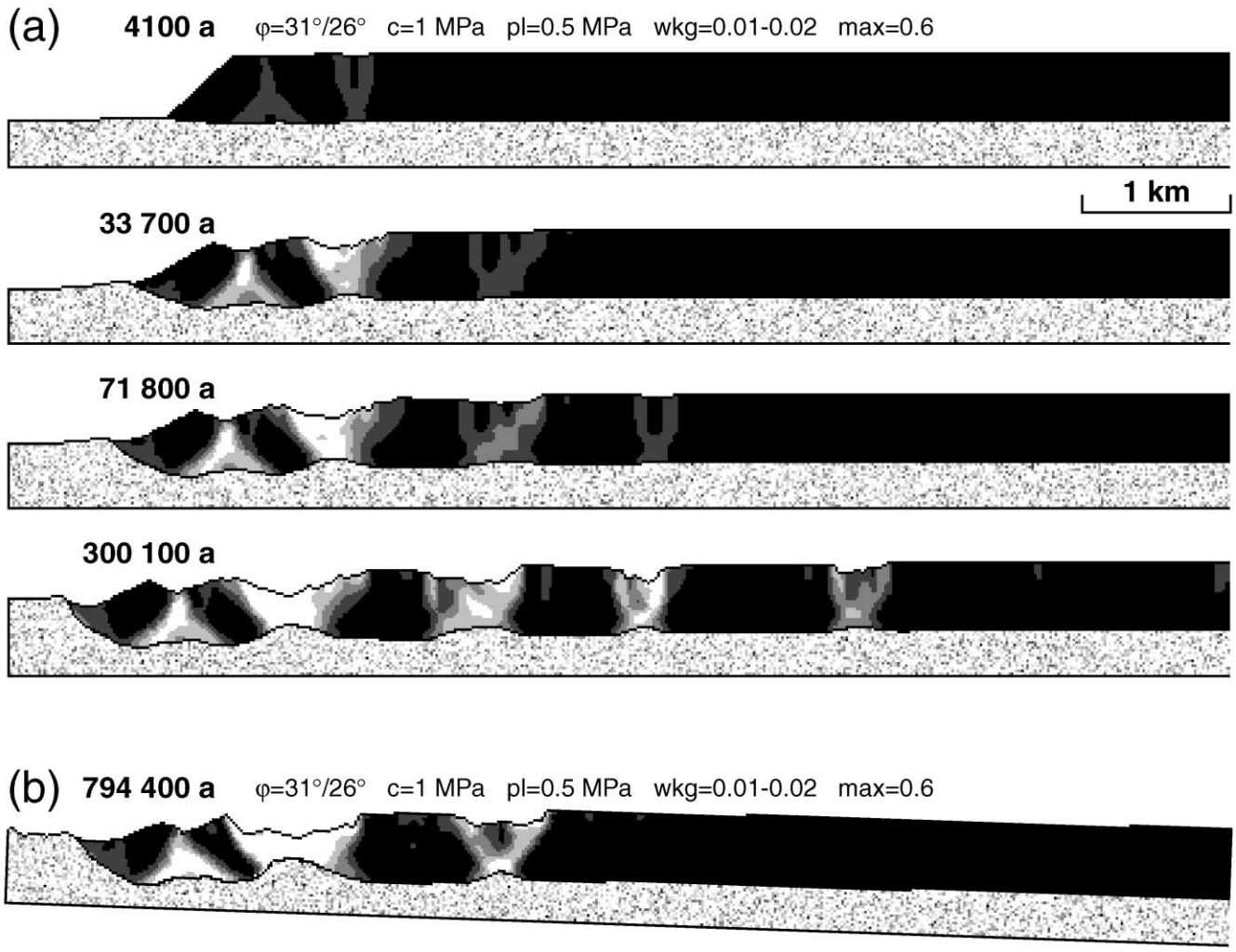

Fig. 14. (a) Sequence of stages in a horizontal model having the same general dimensions and rock properties as the models in Figs. 9b and 10. (b) Model sloping away from the simulated canyon at 2°. Stage shown is after a much longer time than in (a).

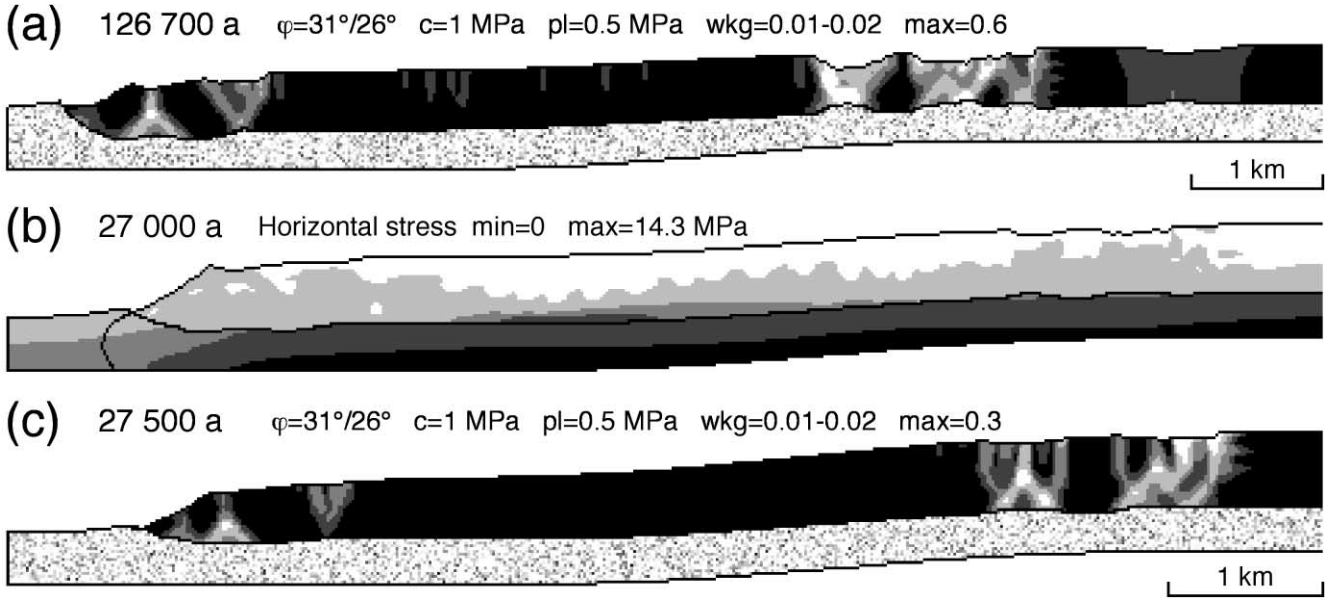

Fig. 15. Model having a slope that increases then flattens toward the river. (a) Plastic strain. (b) Horizontal stress. Areas in white have negative (tensile) stress; areas in black exceed 14.3 MPa. (c) Modified to have overburden thin from 500 m (right) to 350 m (left).

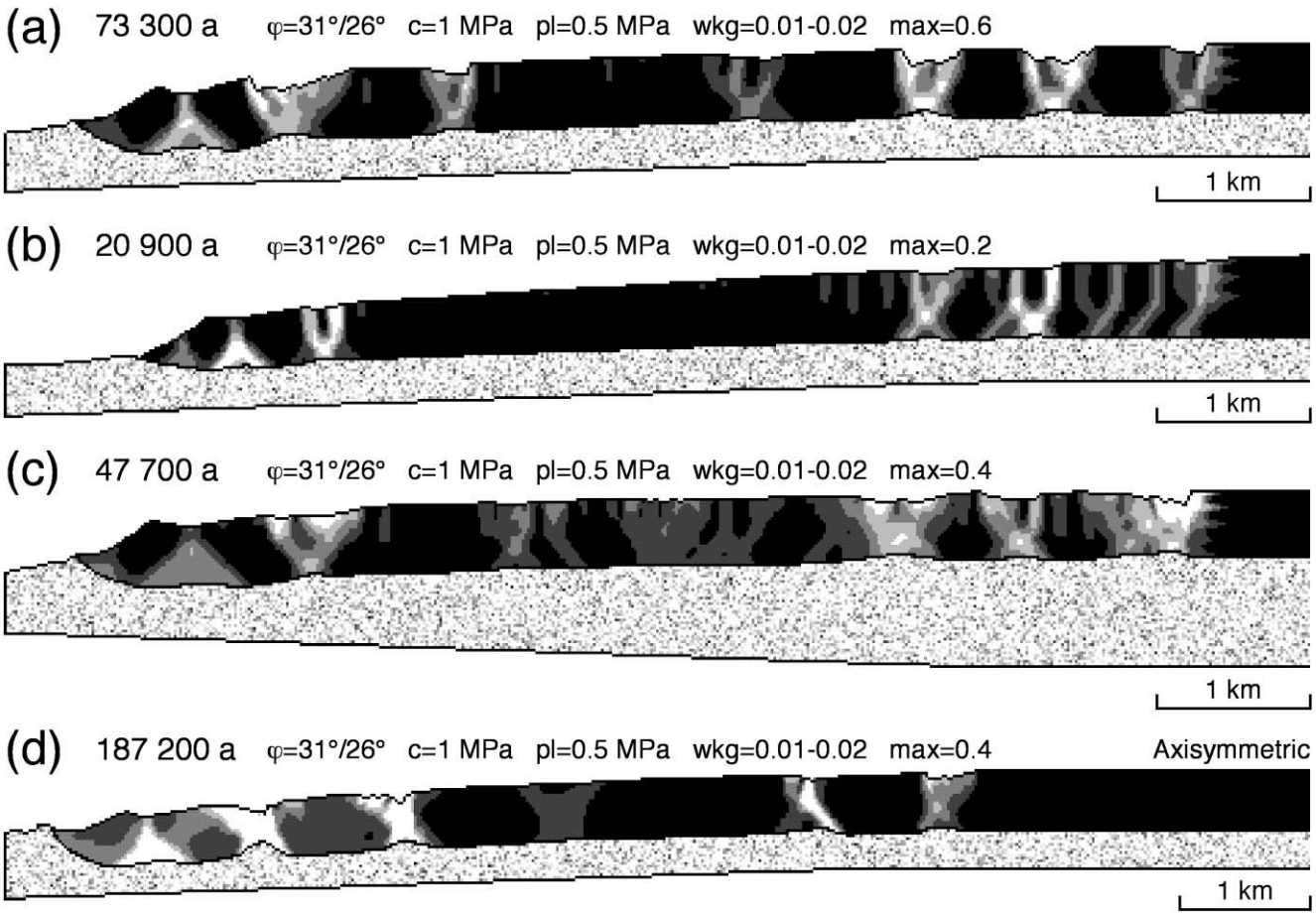

Fig. 16. Models that vary slope. (a) Model that changes from horizontal to a constant 2° slope across a smooth bend. (b) Model in (a) modified to have overburden thin from 500 m (right) to 350 m (left). (c) Model in (a) modified to have salt thin from 764 m (right) to 300 m (left). (d) Model in (a) run as if axisymmetric about a point 5.6 km west (left) of the canyon wall. Out-of-plane stresses due to radial inward movement change the location and intensity of faulting.

Despite the similarity of model and natural structures, not an increasing, a horizontal, or a reverse slope replicates the surface slope observed in Canyonlands. The next models explore other factors that could cause an upslope progression of failure compatible with the observed slope.

The model in Fig. 15 had a smoothly curved slope that steepened, then flattened, toward the river. The curved part approximated a sine curve. Similar to the evolution in the constant-slope models, extension concentrated at the upper slope break. No other part of the overburden extended significantly, except near the rotated and sagged toe. Indeed, the lower part of the overburden shows greatly increased horizontal stress where the slope decreases, thoroughly inhibiting through-going faults. A tendency toward downslope gliding decreases horizontal stress in areas of steepening slope but increases it where the slope flattens. Thus, the generalized slope observed in nature (Fig. 2) cannot alone account for the inferred upslope progression of failure.

To test whether the strength decrease caused by overburden thinning would change the fault pattern, we ran the model in Fig. 15c. The thinning from 500 m regionally to 350 m near the river exceeds the maximum allowed by field data. As the results show, the thinning had little effect — certainly not enough to account for the discrepancy with nature.

The model in Fig. 16a explores the idea that the concentrated faulting at the slope break in Fig. 4 may have been caused by the sharpness of the break. The model here bends smoothly from horizontal to a constant 2° slope. This change did serve to distribute the faulting more, but not as much as in nature, and most of the largest grabens were still at the top of the slope. Overburden that thinned toward the canyon did not change this basic pattern (Fig. 16b).

The model in Fig. 16c tested the effect of salt thickness. In a well about 7 km east of the easternmost graben, the salt thickness is 540 m (Woodward–Clyde Consultants, 1983). An isopach map of the saline facies indicates westward thinning to about 300 m at the river in the north to less than 30 m in the south (Woodward–Clyde Consultants, 1983, fig. 15-12). Because our models are optimized for the northern part of The Grabens, the expected thickness change beneath the extended sheet is about 100 m. The model in Fig. 16c used opposing 2° slopes on the top and

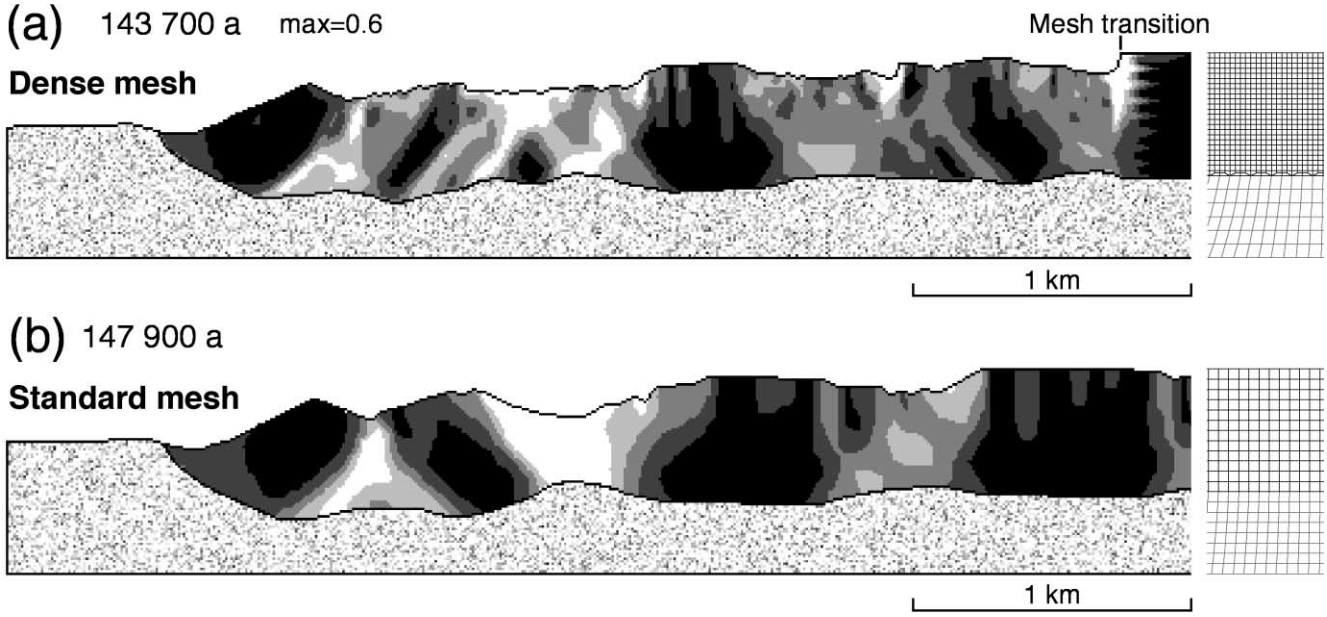

Fig. 17. Results of different overburden mesh spacing in horizontal models. The model in (a) has 24 square elements vertically in the overburden versus the standard 12 elements in (b). Grid to the right of each model shows a representative portion of the overburden mesh. Bottom row of mesh in (a) shows transition to salt elements that were twice as large.

base of salt to vary its thickness from 764 to 300 m. This change altered the faulting pattern somewhat (compare with Fig. 16a), but again not nearly enough to agree with the natural pattern.

The curved trend of the natural grabens (Fig. 1) creates converging circumferential displacement as the overburden moves radially toward a point to the west of the river. Our software can simulate axisymmetry in addition to plane strain. The model in Fig. 16d assumed axisymmetry about a point 5.6 km west from the canyon wall, determined by fitting arcs to the trends of the grabens on the geologic map. Otherwise, the geometry was identical to that in the model in Fig. 16a. In comparison, the axisymmetric model developed much less extension at the upslope end and showed more tendency to fault in the central part of the slope. Apparently the crowding of the rocks as they move westward and radially inward increases the graben-parallel stress and tends to inhibit extension. Extension at the free face of the canyon locally relieves the crowding there, but not upslope. Thus, the concentric pattern of the grabens may partly explain the upslope progression of failure.

Although the natural grabens show a roughly axisymmetric pattern, the free face of the canyon and the topographic slope are not similarly curved. Indeed, the southernmost grabens are nearly perpendicular to both. Some other factor must therefore be causing the curved fault trends. Clearly, the problem needs to be considered in three dimensions. Physical models have convincingly demonstrated how frictional lateral boundaries influence fault patterns (e.g. Vendeville, 1987). Extensional faults form strongly curved patterns concave in the direction of extension if friction restrains extension along the lateral edges. We think the same sort of effect may operate in the natural grabens system. The northern margin of systematic graben faulting corresponds to a change in dip direction adjacent to the canyon (Fig. 5; Huntoon et al., 1982; structure-contour maps in Woodward–Clyde Consultants (1983) and McCleary and Romie (1986)). The detaching salt layers pinch out at the southern margin of the grabens (Fig. 5; Woodward–Clyde Consultants, 1983; Condon, 1997). The zone of graben faulting lies north of the salt pinch-out and within the area where beds dip northwestward at a high angle to the canyon trend (Fig. 5). As noted by McGill and Stromquist (1979), both of these natural edge effects would act as restraining boundaries and retard gravity-driven extension at the margins of the fault system. Extension would initially concentrate equidistant from the edge effects at the canyon wall free surface, then propagate as curved systems both upslope and laterally toward the margins. The physical model of McGill and Stromquist (1975, 1979) developed a similar pattern when the detaching layer of wax was locally softened by heating. Higher viscosity cool wax at the margins of the zone inhibited gliding at the lateral and upslope margins, so that grabens opened sequentially away from the free boundary.

Therefore, the map pattern and propagation sequence of the Canyonlands grabens strongly relate to the boundary conditions in three dimensions. Although the numerical models described here are valid for plane strain or axisymmetry and can reveal much about the mechanical evolution of those grabens, complete simulation of the interaction between slope and edge effects requires fully three-dimensional models.

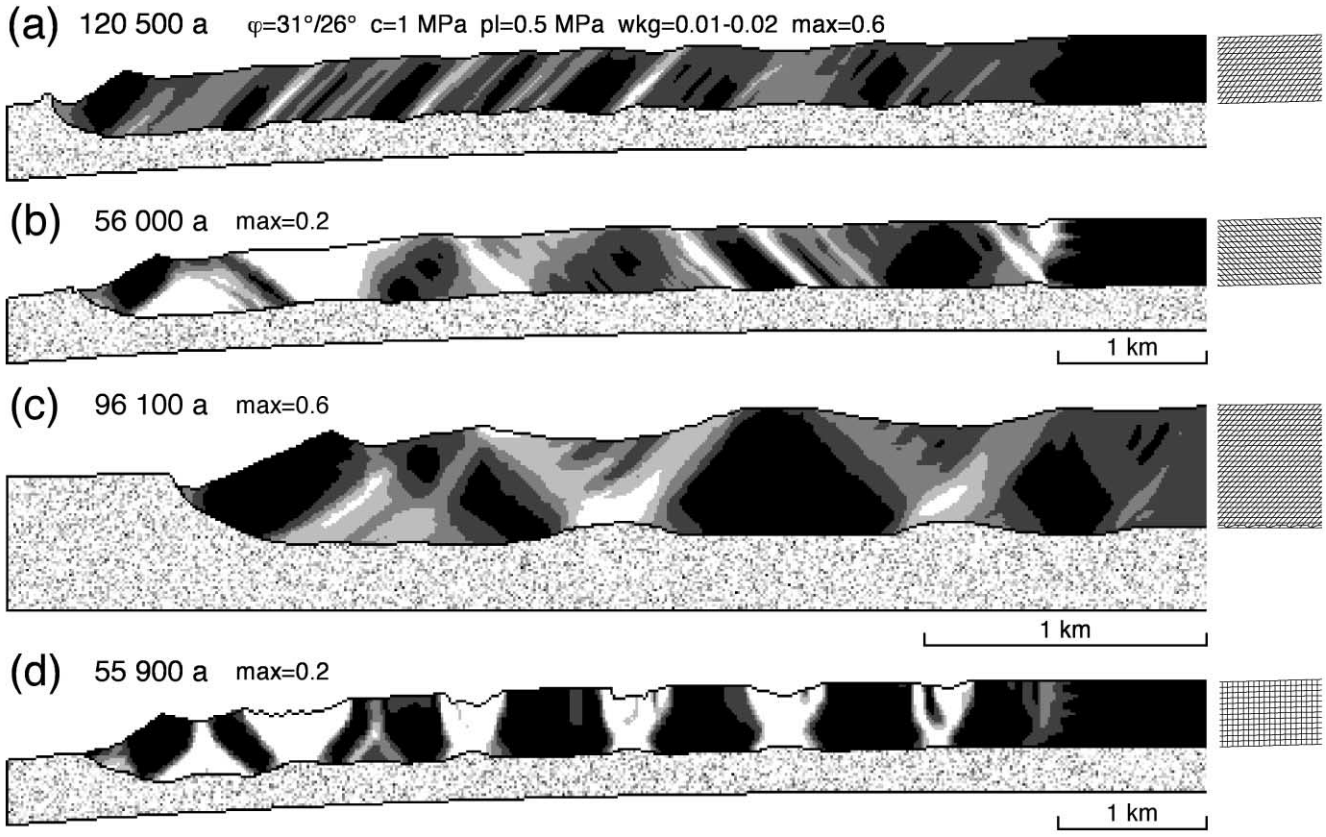

Fig. 18. Results of varied finite element mesh orientations. Grid to the right of each model shows a representative portion of the overburden mesh. Plastic strain is contoured in each model. (a) Model built with grid lines slanted downdip. (b) Model with grid lines slanted updip. (c) Model with grid orientation of (a), but half the grid spacing. Bottom row of mesh shows transition to salt elements that were twice as large. (d) Model with standard horizontal and vertical grid lines for comparison (same model as Fig. 9b).

5.4. Mesh effects

Because finite element models numerically solve the governing equations only at node points and use a simple interpolation between them, the spacing and pattern of those nodes can affect the computed results. This mesh effect appears as a dependence on both the spacing of the node points and the orientation of the mesh that they constitute.

The spacing of the node points obviously controls the resolution of detailed structural variations, but there is also a more insidious effect. Most of the common finite element formulations (including the one used here) do not include any sort of inherent length scale. If the deformation localizes (Hobbs et al., 1990), such as on a shear band representing a fault plane, the finite element method has no criterion for determining the width of that localization other than the node spacing. Thus, the shear band may be arbitrarily thin for a correspondingly dense node spacing. The length scale in natural deformations is determined by inhomogeneities that affect the deformation on some scale, such as grain size or joint spacing. However, beyond the resolution issue, certain numerical relations become pathologic as the limits of mesh spacing are approached. As the spacing is reduced, the strain in the localized shear zone approaches infinity, and the energy dissipation tends to zero (Belytschko et al., 1986). Various mathematical strategies are used to cope with this problem (e.g. Bazant and Belytschko, 1987; Needleman, 1988; Garikipati and Hughes, 2000), but their use is rare in commercially available software and particularly in geological applications.

The mesh size effect is illustrated by halving the spacing of elements both vertically and horizontally (Fig. 17). Although the change appears as an increase in minor faults and some variation in their location, the major structures are similar in their geometry. The location and spacing varies somewhat, but presumably this difference derives largely from the transition in mesh spacing near the right edge of the portion of the model shown in Fig. 17a (see Fig. 3 for an illustration of this type of transition). A graben generally forms at the transition in all models if it is not located far from the area of active faulting. The general similarity of structures despite differences in mesh density arises because the width and spacing of the grabens is controlled partly by the flexural properties of the overburden and flow patterns in the salt. The thickness and elastic properties determine the flexural rigidity of the overburden, which imposes a length scale on the deformation. Thus, the influence of mesh spacing on the modeling results is relatively minor here,

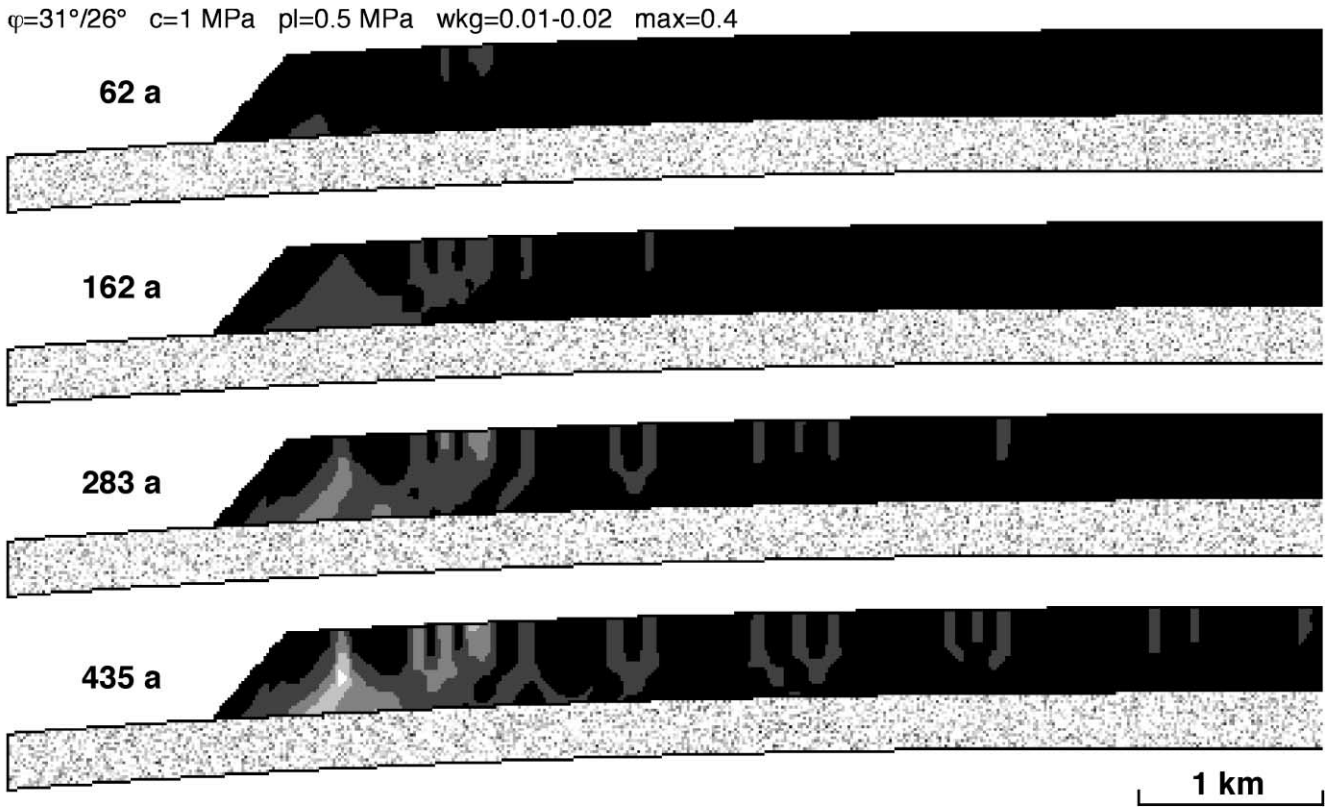

Fig. 19. Early stages of model in Fig. 9b showing initiation of faults at the surface and their downward propagation and intersection.

as long as the spacing is significantly shorter than the dimensions of the major structures.

The overburden in all of the models discussed previously had grid lines that were vertical and parallel to the upper and lower boundaries (Fig. 3). For numerical reasons, failure preferentially occurs along grid lines or diagonally across elements (Tvergaard et al., 1981; Needleman and Tvergaard, 1984; Armero and Garikipati, 1996). Alternatively, an unstructured mesh (no biasing in any direction) is overly stiff to deformation (Armero and Garikipati, 1996), and shear bands are wider (Needleman and Tvergaard, 1984). The mesh-orientation effect is minor in compression but can be significant in extension with strain weakening (Fig. 18). In each of these models, the extensional shear zones were strongly oriented along the grid lines. This effect was particularly evident in the early stages and where the mesh was slanted in the slope direction (Fig. 18a). As extension accumulated and the structures grew, diffuse antithetic faults propagated to create more-symmetric grabens (Fig. 18a and c). Increased node density decreased the effect (Fig. 18c).

Clearly mesh orientation strongly influences the model. Because removing its effect is not simple, however, the effect remains an unavoidable limitation to our numerical models. In defense of the results for The Grabens area of Canyonlands, we note that the Cedar Mesa Sandstone in the upper part of the section is massive but strongly dissected by vertical joints (Stromquist, 1976). The joint control on fault traces at the surface is obvious throughout the area (Stromquist, 1976; McGill and Stromquist, 1979). The influence at depth is less clear. This jointing introduces a major mechanical anisotropy in the rocks that strongly favors vertical faulting in the upper section. We argue that the mesh effect for the vertical mesh has the same influence. Therefore, although the mesh effect is significant, it may actually bias the model results in the same way that the preexisting joints did in nature.

6. Mechanics of graben growth

The detailed mechanics of the fault-pattern evolution are complex, even for the simple horizontal models. The mechanical controls on fault propagation and spacing will be discussed fully in a future paper. Here we summarize the major features, particularly as to how they relate to past debates about propagation direction and the effect of the flowing viscous substrate.

6.1. Fault initiation

The horst and graben near the canyon in the models form almost immediately, driven by salt spreading westward and bulging upward into the canyon. This flow rotates and flexes the overburden. Faults originate where bending stresses

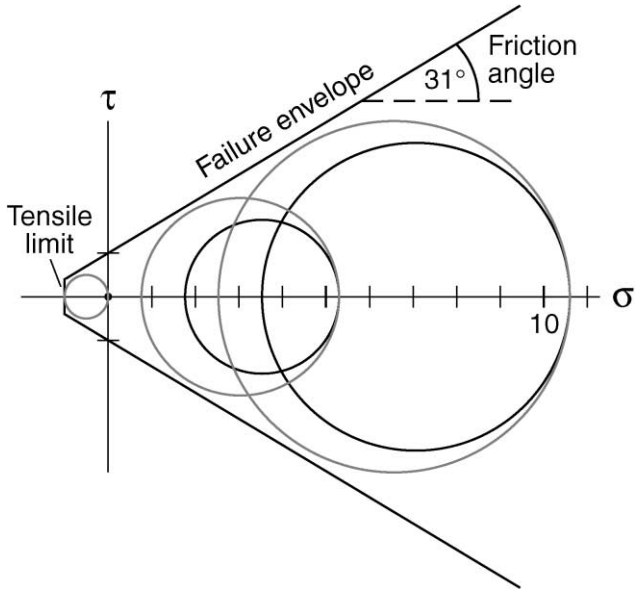

Fig. 20. Mohr diagram showing stress states before and after horizontal stress release by downcutting. The black circles show initial stresses (in MPa) at the bottom surface (right), middle (middle), and top surface (dot at intersection of axes) of the overburden, assuming horizontal stress is one-third of vertical stress (see text). Gray circles show the effect of uniform release of horizontal stress, representing instantaneous downcutting of the canyon. The top surface reaches the tensile limit when horizontal stress is reduced by 1 MPa, as shown. The other locations have not reached failure. Thus, failure tends to initiate at the top surface.

reduce the horizontal stress in the overburden the most. Upward flexure at the canyon wall decreases stress at the base, and horst faults propagate up from there. Salt expelled from beneath the overburden causes that area to subside and flex downward immediately upslope, initiating a graben propagating downward next to the horst. Fig. 9b shows a mature stage of this horst-graben pair.

Younger grabens that grow upslope form by a combination of extension driven by gravity spreading and flexure caused by progressive expulsion of salt toward the canyon.

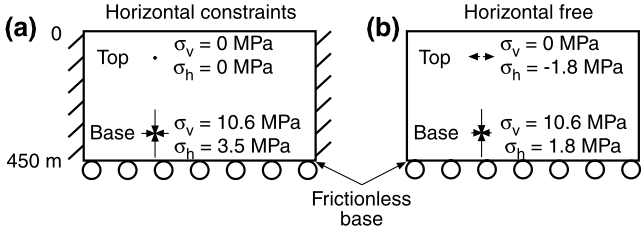

Fig. 21. Blocks showing change of stress state caused by release of horizontal constraint. (a) Block stressed by gravity between horizontal constraints. The stresses at the top and bottom of the block are noted and are plotted on the Mohr diagram of Fig. 20. (b) Complete release of horizontal stress above a frictionless base leaves the vertical stress unaffected but decreases horizontal stresses to be equal and opposite at the top and bottom to maintain equilibrium. Fig. 20 shows that the failure envelope is reached at the top surface before horizontal stress is completely relaxed. Friction or salt drag would decrease the amount of stress reduction on the base.

A future paper will detail the controls on this process and how properties of both salt and sedimentary rock control the graben spacing. But here, suffice it to note that the modeled graben faults all originate at the top surface and propagate downward (Fig. 19). Short vertical faults appear all along the top surface, reflecting the tensile stress limit in the failure criterion. Only a few of these eventually grow downward, where they decrease in dip to form shear faults and converge to outline grabens. This transition from tensile to shear failure represents the Type B propagating tips of Cartwright and Mansfield (1998). The two bounding faults of a graben form and grow nearly, but not precisely, simultaneously. As shown by Melosh and Williams (1989), flexure caused by slip on one normal fault greatly increases the probability of adjacent failure. A very small slip on the initial fault perturbs the stress sufficiently to induce the companion fault of a graben, such that the graben appears to grow as a single structure. This mechanical analysis echoes descriptions by Heiskanen and Vening Meinesz (1958) and Vendeville and Jackson (1992). Therefore, the mechanical properties of the rocks determine the width of the grabens. Initiation of the graben faults upward from their intersection point is not required to create consistent grabens, as presumed by McGill and Stromquist (1975, 1979).

Initiation of faults at the surface and their downward propagation are also predicted by a simple stress analysis. The system in Canyonlands represents an unusually straightforward perturbation of the regional stress field (Fig. 20). Vertical stress would be due only to the lithostatic load and near uniformity laterally. Therefore, assuming the model density of 2400 kg m^{-3} for the overburden, the vertical stress would increase from zero at the surface to 10.6 MPa at 450 m depth. The prefaulting horizontal stress is unknown. For simplicity, we ignore the slight dip of the overburden. A plausible minimum would be the horizontal constraint condition, where horizontal stress is one-third of the vertical stress (for a typical Poisson's ratio of 0.25, as in the models), as shown in Figs. 20 and 21a. More likely, the horizontal stress would be close to the vertical stress (McGarr, 1988; Banerdt, 1990). Downcutting of the river must have released horizontal stress almost geologically instantaneously because the topography appears to be relatively unchanged by widespread erosion. The canyon incision would release the horizontal stress at the canyon wall progressively from the surface down. Given the most conservative scenario of instantaneous downcutting and frictionless base, horizontal stress would decrease equally at all depths within the overburden (stresses are more complicated near the free face, where horizontal stress is zero). For a purely elastic overburden, the end result would be equal (absolute value) tensile and compressive horizontal stress at the top and base, respectively, at a magnitude one-half the initial basal stress (Fig. 21b). This state may also be viewed as uniform reduction by the mean initial horizontal stress. For an elastic–plastic rock, however, the failure

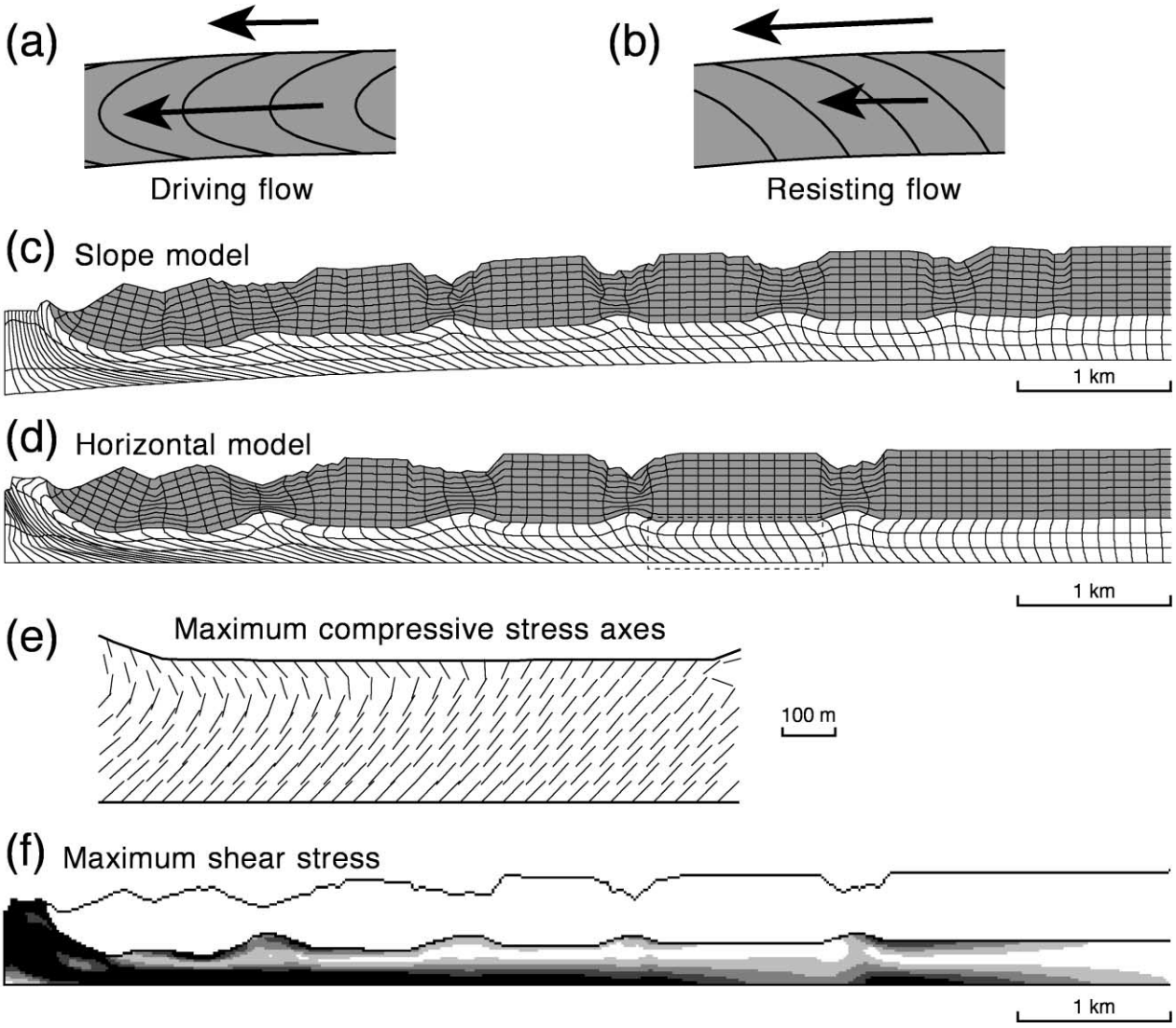

Fig. 22. Deformation of passive material lines in salt indicates relative motion of salt and overburden. Idealized patterns show salt actively driving (a) or resisting overburden extension (b). (c) and (d) show deformation of grids of passive material lines that were initially vertical or parallel to the bottom boundary. Initial spacing was 100 m horizontally, 100 m vertically in the salt, and 50 m vertically in the overburden. Salt flow in slope model (c) indicates that salt resists overburden extension. Salt flow in horizontal model (d) shows resisting flow at the front part but minor driving flow at the rear. (e) Orientation of maximum compressive stress directions within the dashed box in (d). (f) Contours of shear stress in salt, ranging from less than 25 (white) to more than 100 kPa (black).

envelope is intersected prior to complete stress release. The failure criterion is reached first at the surface, especially with a tensile-stress limit (Fig. 20). Larger, preexisting horizontal stress would enhance this tendency, as would slower or incomplete downcutting, viscous drag from underlying salt that resists extension (see next section), and downward flexure of the toe of the overburden due to salt expulsion.

Initial failure at the surface on vertical planes (tensile-stress limit) would appear similar to that of the joints in the field. Thus, the preexisting joints should not have affected the general form and propagation direction of the faults in cross-section. Indeed, models run with and without initial vertical 'joints' (surfaces of no horizontal stress) produced nearly identical results. Of course in three dimensions the strike of the joints would interact with the lateral fault propagation, as noted by most previous workers.

Rock in the models beyond the zone of active faulting has stresses corresponding to the Mohr–Coulomb active-limit state (defined in Mandl, 1988) after release of horizontal stress at the canyon. That is, the unfaulted slab is at the failure envelope throughout. Only small stress perturbations are needed to drive or inhibit faulting. This state suggests the question: why does the entire overburden not fail by faulting simultaneously? The answer derives from the existence of the viscous substratum, which also must deform as the overburden extends.

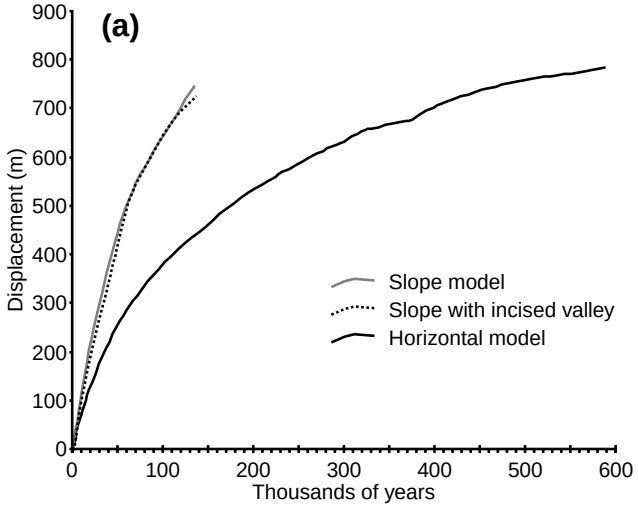

Fig. 23. Total displacement history for sloping (Figs. 9b and 10) and horizontal (Fig. 14) models.

6.2. Salt flow

Agreement does not exist on the role of the salt layer in the formation of the Canyonlands grabens. The presence of salt is acknowledged by all workers to be necessary for extension and faulting. However, the amount of salt flow and whether salt flow drives or resists the extension have not been conclusively demonstrated.

Baker (1933) thought that faulting was driven by salt flowage into the river canyon to form the Meander Anticline. McGill and Stromquist (1979) agreed that salt flow was integral to the structural evolution, but its role as either driving or resisting the extension was not clearly stated. They argued for 'little or no shear stress' on the base of the overburden. Huntoon (1982) hypothesized a 'décollement' of 'viscous shearing' at the top of the salt, with salt flow 'incidental' to the development of the faulting. Similarly, Ely (1987) attributed extension to lubrication of the top surface of the salt by water infiltrating fault planes. Moore and Schultz (1999) inferred salt-flow features, such as reactive and active diapirs, in addition to the valley anticlines noted by others (Potter and McGill, 1978).

If the numerical models described here represent reasonable simulations of the natural system, they contain abundant information on the operative mechanics. Flow of salt within the layer allows extension over reasonable time spans (on the order of 100,000 years) for realistic geometries and rock properties. No unusually weak décollement at the top salt surface is required.

Inspection of the deformation of passive material lines unambiguously constrains salt's role as driving or resisting extension of its roof. Distinguishing factors are: (1) relative displacement of salt and overburden, and (2) where the maximum displacement is in the salt. If salt actively drives the overburden extension, the maximum flow should be well below the overburden contact and show decreasing flow toward the contact (Fig. 22a). Such a flow pattern typifies viscous flow in a stationary pipe or channel. If the salt resists overburden extension instead, the material lines should have maximum displacement at the contact (Fig. 22b).

In general, passive grid lines in the modeled salt indicate that it resists overburden extension in the models (Fig. 22b–d). In the slope model (Fig. 22c), the only perturbation to this pattern was caused by local flow into the reactive diapirs below grabens. The pattern in a horizontal model showed more variability (Fig. 22d). The salt clearly resisted overburden extension near the canyon, where spreading was the most active. Away from the canyon, the overburden load expelled salt laterally from nonextending parts of the overburden and created a pattern of salt flow driving the extension.

Orientation of principal stresses in the salt reflects the change from resisting to driving flow (Fig. 22e). Shear stress shows a clear minimum in the center of the salt layer (Fig. 22f) in areas of driving flow (e.g. right-hand portion), whereas shear stress decreases upward more uniformly in areas of resisting flow (center portion) (the upward decrease in lithostatic pressure imposes a general upward decrease in shear stress, even where it is otherwise unperturbed). Where the principal stress axes are nearly 45° to the salt contact, the maximum shear stress is parallel to the contact, and the contours in Fig. 22f reflect the contact-parallel shear stress. The shear stress along the contact is generally less than 0.1 MPa in this horizontal model (Fig. 22f). Thus, as inferred by McGill and Stromquist (1979), the shear stresses are indeed low parallel to the contact. The largest Mohr circles in Fig. 20 indicate maximum stress values two orders of magnitude larger in the overburden at its base. In the overburden, the maximum compressive stress axes are nearly perpendicular to the contact, so shear stress along the contact is a small fraction of the maximum shear stress on the order of 4 MPa (Fig. 20). The situation is similar in the slope models.

General resisting flow in the salt is required by the time dependence of the rocks involved. Deformation in the brittle overburden is independent of time in the models and is likely nearly so in nature. The only time-dependent deformation is in the viscous salt. Because gravity is the driving force and remains constant, once the overburden reaches the failure criterion, deformation would be instantaneous and indefinitely large in the absence of salt (e.g. on a frictionless base). The salt resists this runaway deformation because stress in it increases as the deformation rate increases. Therefore, as demonstrated in the models, salt flow regulates deformation in the overburden instead of driving it. Because the governing salt flows fastest where the pressure gradient is largest near the free surface of the canyon, faults originate progressively away from the canyon in the horizontal models. The situation is more complicated in the dipping models, because, as discussed earlier, the stress in the overburden varies laterally.

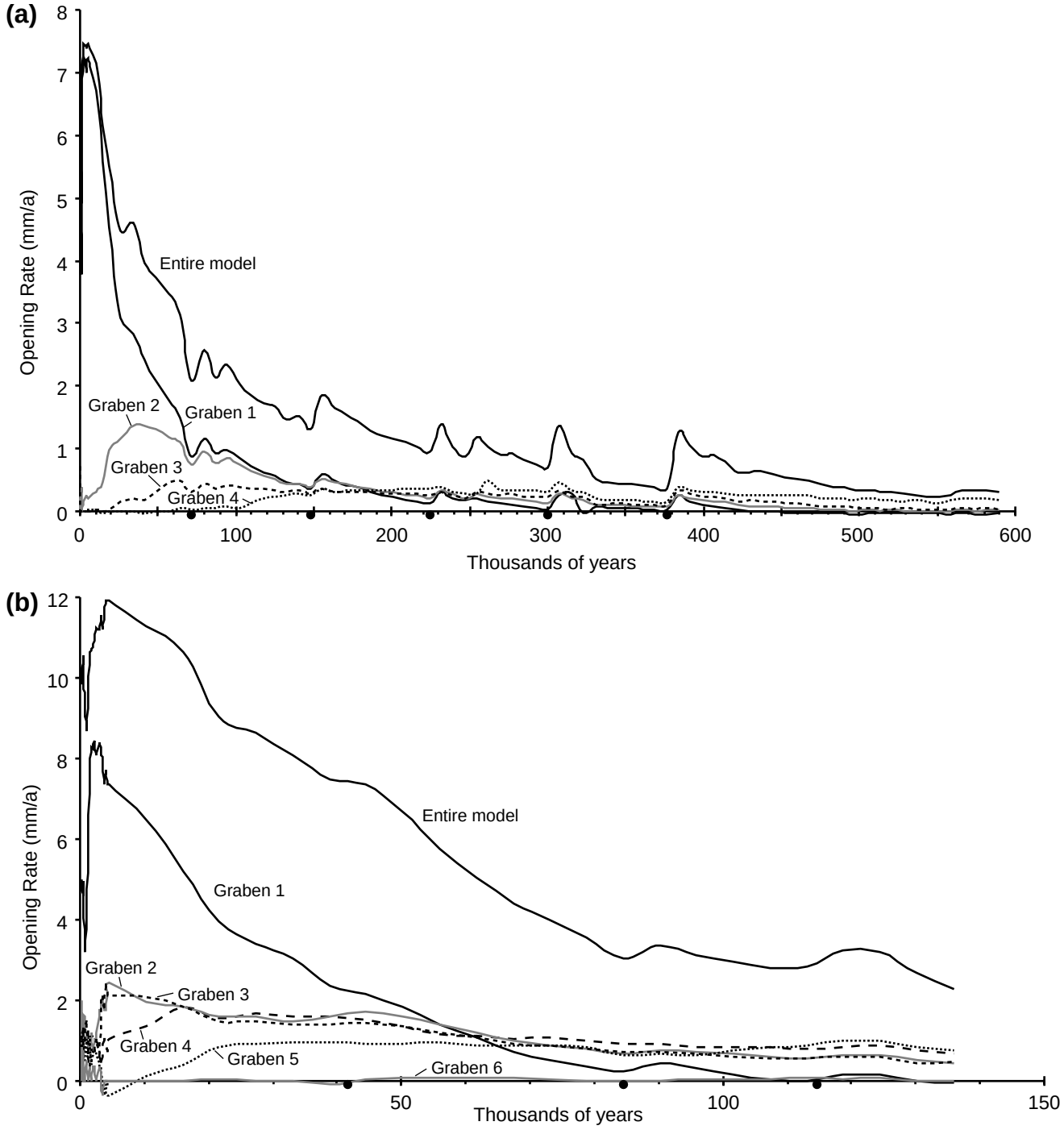

Fig. 24. Graphs of spreading rates across individual grabens in the: (a) horizontal (Fig. 14), and (b) sloping (Fig. 9b) models. Curve labels correspond to grabens increasingly farther from the canyon. Dots on the bottom axes mark times of removal of a layer of salt elements ('erosion'). Fluctuations in the early stages derive from round-off errors in distance measurements relative to short time periods between data output. The number of data points varied between models. During the major part of the models' history (after about 5000 years), the slope and horizontal models had 23 and 78 points, respectively. The horizontal model, however, ran about four times the total time of the sloping model. Fewer points dampen the apparent amplitude of peaks and troughs in the curves.

6.3. Rates and amounts of extension

The slope models attain a maximum surface relief of about 200 m (Fig. 10) but generally no more than about 100 m (Fig. 9b). That relief roughly matches the exposed relief in the field, but an unknown thickness of alluvial fill (Moore et al., 1997) indicates significantly greater structural relief there. Therefore, the models have most likely not extended as much as the natural grabens. Our estimate would be about 25% less.

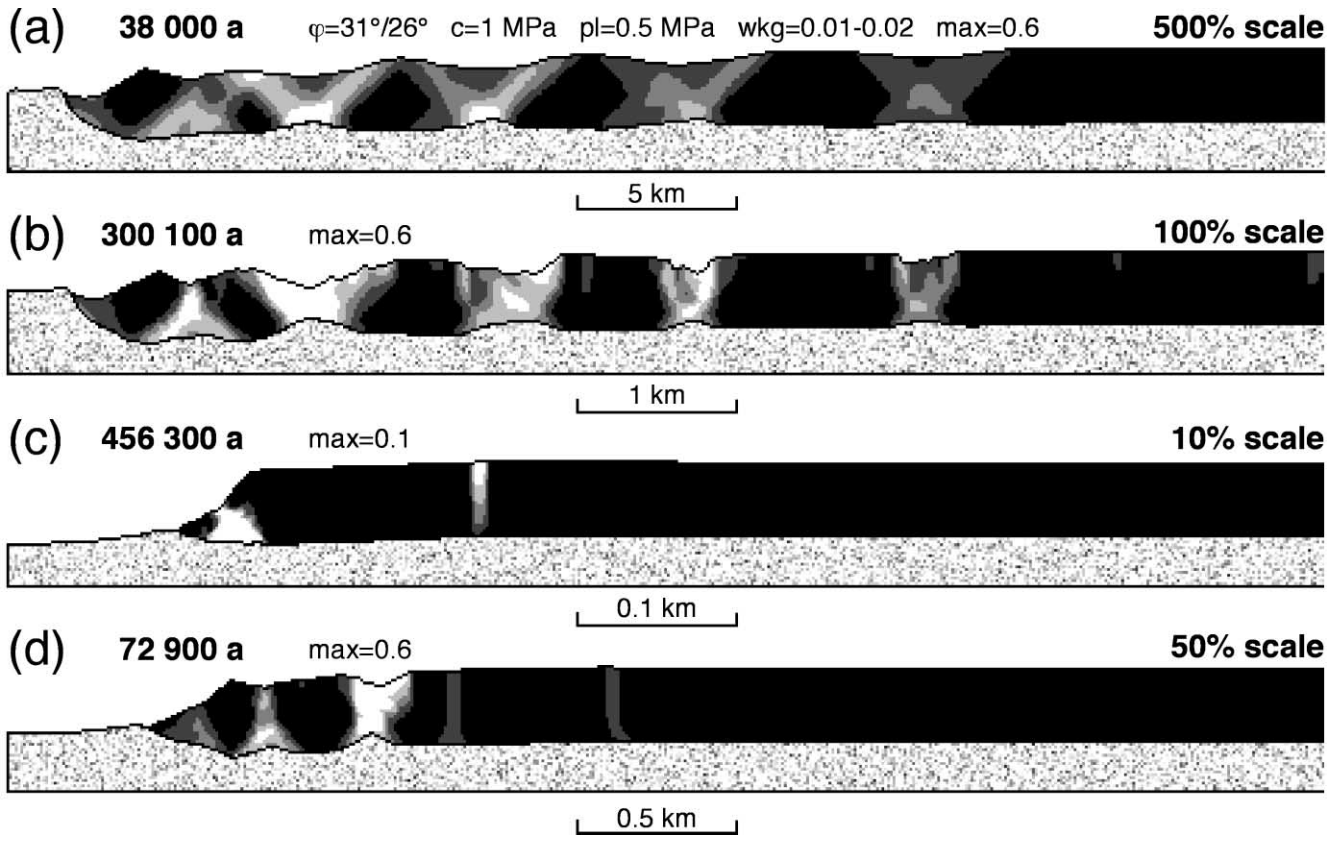

Fig. 25. (a) Strain contours for a horizontal model five times larger in scale than preceding models. (b) Standard model for comparison. (c) Model ten times smaller in scale and after a longer time. (d) Model twice as small in scale as that in (b). All models have the same rock properties.

Duration of extension in the models depends on the slope, length, and material properties. The most realistic models attained their maximum deformation in about 135,000 years (Figs. 9b and 10). Further extension was inhibited by proximity of the overburden tip to the left boundary and large distortion of the finite element mesh. The first factor would not affect the natural grabens because the canyon walls are continually eroded and carried away by the river. General correspondence between duration of the models and dating in the natural grabens (Biggar, 1987; Biggar and Adams, 1987) indicates that the viscosity chosen for the salt is appropriate.

Extension in the models slowed with time (Fig. 23), caused by: (1) narrowing of the exposed salt surface in the canyon, which inhibited upwelling of the salt there; (2) increasing length of extending overburden, which increased the length of moving salt and thereby the viscous resistance; and (3) thinning of the salt layer by expulsion into the canyon.

Strain measures depend on the length of the model used for the undeformed reference. We measured from the node at the rightmost extent of deformation in the final state to the tip of the horst on the left (the tip of the horst was used to avoid complications from the large rotation of the block at the canyon wall). Initial lengths were 5.21 and 4.16 km for the sloping and horizontal models, respectively (Figs. 9b and 14a). These reference lengths are the shortest possible, so the strains and rates calculated are the maximum for each model.

Strain rate varied from about $7 \times 10^{-14}\,s^{-1}$ to $1 \times 10^{-14}\,s^{-1}$, well within the range of typical geologic rates. Maximum extension was about 14–18% for the sloping and horizontal models, respectively. The actual displacements were about 750 m for the horst tip of both models; the strains differ because of the different reference spans. The structural development appears similar to that shown in the topographically precise cross-section in Moore and Schultz (1999), who calculated 25% extension. Their initial length was 5.18 km, very close to ours. The discrepancy between the model results and the Moore and Schultz (1999) estimate most likely results from two factors. First, the extensions calculated and modeled depend sensitively on the dip of faults. The field measurements require inferred dips projected down from surface exposures. Fault dip in the models depends on material properties. Second, the cross-section of Moore and Schultz (1999, fig. 13) requires unusual movements to restore the largest graben. Blocks appear to require horizontal sliding and stacking, judging from the position of the reference line. Drawing their cross-section with reactive grabens (Schultz-Ela and

Jackson, 1996) that are restorable above diapirs (such as in Vendeville and Jackson (1992), figs. 7 and 8) would decrease the calculated strain.

The extensional strain rates of the models can be expressed as displacement rates to assess the potential for directly measuring displacement in the field. The incremental displacement rate for the tip of the horst varies from 12 mm a^{-1} (initial) to 1 mm a^{-1} (final) for the entire models (Fig. 24). Slope breaks in the curve record erosional events in the canyon floor, which rejuvenated the spreading. This behavior underscores the dependence of spreading rate on differential load (relief) and not just the tilt of the model. Sloping models had faster spreading rates but always less than double those of the horizontal models.

Displacement rates across individual faults or grabens were less than for the entire models (Fig. 24). Spreading rates across grabens, calculated as the change in distance between nodes in undeformed blocks on either side of the grabens, ranged from a maximum of 7 mm a^{-1} to more typical rates of 2 mm a^{-1} or less (Fig. 24a). The plot of displacement rates across individual grabens in the horizontal model (Fig. 24a) nicely shows sequential initiation and growth of grabens away from the canyon, all part of an overall declining spreading rate. Initially, spreading rate quickly accelerated to a maximum, which was almost entirely due to extension across the first graben. Displacement across the second graben accelerated as the rate decreased on the first graben. Similarly for the third and fourth grabens, although they did not show a significant fall off in opening rate after their maxima. Thus, the grabens away from the canyon progressively became the dominant contributors to the total extension rate. The period of accelerating rate was longer and the peak rate was lower for each successive graben. The first graben, and less so the second, were the most influenced by salt elevation in the canyon. As the level rose, owing to salt expulsion from beneath the overburden, the extension rate decreased and became even slightly negative (minor shortening). Erosion of some of the salt markedly increased the spreading rate there to nearly the same as that of the more consistently extending grabens away from the canyon.

Opening rates across individual grabens in a sloping model (Fig. 24b) also increased sequentially, but in a shorter time than in the horizontal model. The first three grabens reached their peak spreading rates within 5000 years after gravity was applied to the model. The model having the initial incised valley (Fig. 10) developed similarly, except that the spreading rate across the valley decreased more slowly and the nearest graben slowed more quickly. Slow initial extension across the upslope grabens (numbers 5 and 6 in Fig. 24b) dropped and even changed to minor shortening as extension across the downslope grabens peaked. It appears that tension throughout the overburden was relieved by growth of the first three grabens, which allowed relaxation and even contraction upslope. Later, the upslope grabens showed faster acceleration and overall higher rates than in the horizontal model (Fig. 24a). As in that model, the grabens away from the canyon changed from minor to major contributors to the total extension rate through time. All extension on graben 1 ceased in the later stages.

6.4. Scale effects

Three models were run to investigate the dependence of structural development on dimensional scale. The first model scaled all dimensions larger by a factor of five while keeping other properties the same (Fig. 25a). The dip of the graben-bounding faults at the surface was the only noteworthy difference from the standard horizontal model (Fig. 25b). No significant vertical portion of the faults appeared in the shallow overburden because the thickness of rock failing at the tension limit was a five times smaller fraction of the overall thickness. Otherwise, features such as relative spacing of the grabens, growth of reactive diapirs, and sequential structural development were all virtually identical to the standard model. For a fivefold increase in dimension, the equivalent structural development should be reached five times faster (Weijermars and Schmeling, 1986; Weijermars et al., 1993). Because five times more displacement should happen in five times less time, the velocity in the larger model should be 25 times greater. In the first 5500 years of the standard model, the horst tip moved at an average of 7.1 mm a^{-1}. For the roughly equivalent scaled time period (five times less), the larger model extended at 187 mm a^{-1}, for a 26-fold difference, which is very close to that predicted. Later in the evolution, the larger model moved nearly 32 times faster. We attribute this departure from exact scaling to the slightly different fault geometries. However, these models demonstrate that scaling relationships (Weijermars and Schmeling, 1986) generally hold for a simple increase in dimension when all rock properties are held the same.

Scaling the dimensions 10 times smaller dramatically changed the results (Fig. 25c). Stresses in the overburden were generally insufficient to reach failure, except on a single vertical fault and a small horst beneath the tip wedge. The vertical tensile fault acted as a hinge, beyond which the overburden tilted down as salt was expelled into the canyon. Obviously the change in structural development invalidated normal scaling relationships with the standard model. Scaling the dimensions by only half (Fig. 25d) diminished the differences. The flexurally induced horst and graben near the canyon grew much like those in the standard model (Fig. 25b) but narrower. The extensional structures farther away grew as tensile failures most of the way down through the overburden. Only at the base did they curve into a shear-failure orientation. Two faults accommodated the extension rather than the multitude of faults in the standard model.

7. Conclusions

The grabens in Canyonlands National Park formed and extended as the overburden spread downslope when the Colorado River cut through it into the underlying salt. Two-dimensional, finite element models illustrate the mechanics involved in the deformation and constrain the possible rock properties.

Complexity and size indicate that the natural grabens sequentially originated upslope away from the river canyon. Models having a variable slope similar to that of the natural grabens or a constant slope showed maximum extension at the top of the slope rather than near the canyon, as in the natural system. The models required either a progressively increasing slope or no slope to reproduce the natural progression of deformation. Boundary conditions in the third dimension are apparently responsible for the difference from the models.

The models show that the fault pattern depends sensitively on the rock properties in the overburden. The structures produced that best matched the natural structures resulted from rock properties typical of laboratory measurements, scaled for the size of the rock mass. The best models had an initial friction angle of 31° and a cohesion of 1 MPa. Cohesion disappeared and friction angle decreased to 26° from 0.01 to 0.02 strain to mimic the strain weakening during natural faulting. A tensile stress limit was necessary to reduce the width of the modeled grabens and to reproduce the vertical upper portion of the observed faults. Salt viscosity of 1×10^{18} Pa s simulated extension rates that fall in the range of natural age constraints.

Adding a predeformation valley to the top of the model improved its realism. A previously unrecognized horst near the canyon has been found in the field that corresponds to the horst in the models formed by flexure as salt flows from under the overburden and wells up into the simulated canyon.

The extensional graben faults form at the top of the overburden and propagate downward. Both faults bounding individual grabens initiate nearly, but not exactly, simultaneously. Downdropping of the graben blocks creates relief that causes salt to rise beneath the grabens as reactive diapirs. The models suggest that the natural grabens have multiple faults on each side.

The viscous salt resists and controls the rate of spreading of the overburden, except beneath the undeformed part of horizontal models, where salt drives the extension. Opening rates across modeled grabens are typically 1–2 mm a^{-1}, although rates may be several times higher early in the history near the canyon. Strain rates across the whole graben array range from 6.0×10^{-14} s^{-1} to 0.5×10^{-14} s^{-1}.

The model results scale well to larger dimensions, except for the steep upper part of the faults. Reducing the dimensions increases the fraction of the overburden failing in pure tension, which is expressed as vertical faults. Driving stresses are also reduced, such that substantially thinner models fail in fewer and more widely spaced locations.

Acknowledgements

Many thanks to Martin Jackson for discussions and thorough reviews of this paper, and to Juliet Crider and an anonymous reviewer for helpful suggestions on the manuscript. We also enjoyed and benefited from discussion in the field with Rich Schultz, Jason Moore, George McGill, and Joe Cartwright. This work was supported by the Texas Advanced Research Program under Grant no. 003658-0035-1997 and by the members of the Applied Geodynamics Laboratory Consortium, namely, Agip Petroleum, Amoco Production, Anadarko Petroleum, BHP Petroleum (Americas), BP International, Chevron Petroleum Technology, Conoco, Exxon Production Research, Louisiana Land and Exploration, Marathon Oil, PanCanadian Petroleum, Petroleo Brasileiro, Phillips Petroleum, Saga Petroleum, Shell Oil, Statoil, Texaco Exploration and Production, Total Minatome, and Vastar Resources. This paper is published by permission of the Director, Bureau of Economic Geology, The University of Texas at Austin.

Appendix A. Numerical code and constitutive relations

We used the software GEOSIM-2D for the numerical modeling. This finite element code simulates plane strain or axisymmetric problems using quadrilateral isoparamtric elements having four nodes (Fig. 3). The code includes various rezoning capabilities, which allow smoothing of mesh distortions during large deformation and removal or addition of elements. Rezoning was generally only used in the salt layer, where we periodically removed a layer of elements as salt flowed into the canyon and smoothed the local distortion of the mesh.

The salt deformation was simulated using a linear viscoelastic constitutive law. Variables were chosen so that behavior was that of a Maxwell solid (e.g. Fung, 1977). The elastic response is specified by bulk modulus and instantaneous shear modulus values. The creep response is defined by the same shear modulus and a relaxation time. Viscosity is the product of the instantaneous shear modulus and the relaxation time. Because salt does not have a long-term yield strength, there is no long-term elastic modulus.

The sedimentary rock overburden was simulated using an elasto–plastic constitutive law. The Mohr–Coulomb failure criterion is most commonly used in geology for pressure-dependent frictional deformation. However, this criterion presents a difficulty for numerical analysis because it does not depend on the intermediate principal stress. Although most of the models are plane strain, nonzero stresses exist in all three dimensions. If the Mohr–Coulomb failure envelope is plotted in three-dimensional principal-stress space, it forms an irregular hexagonal pyramid centered on the

mean stress axis. The mean stress is the first invariant (I_1) of the stress tensor, and equals $3p$, where p is pressure. The numerical problem arises if the stress reaches one of the corners on the failure envelope: there, the plastic flow vector is not uniquely defined. Our modeling uses the closely-related Drucker–Prager failure criterion (Drucker and Prager, 1952) instead, which smoothes the Mohr–Coulomb failure envelope into a circular cone centered on the mean stress axis. Dependence on the intermediate stress is minor, calculation of failure conditions is numerically efficient, and the flow vector is uniquely defined everywhere on the failure envelope. Good descriptions of these failure criteria and their limitations can be found in Chen and Han (1988), Vardoulakis and Sulem (1995), and Barnichon and Charlier (1996).

The Drucker–Prager yield criterion, F, is defined as:

$$F(I_1, J_2) = \alpha I_1 + \sqrt{J_2} - k = 0,$$

where I_1 is the first invariant of the stress tensor, J_2 is the second invariant of the deviatoric stress tensor, and α and k are constants. For convenience, let $T = \sqrt{J_2}$. Then the Drucker–Prager failure envelope plotted on p and T axes appears similar to the Mohr–Coulomb envelope on normal stress and shear stress axes, respectively. Analogous to cohesion (c), k is the intercept with the T axis and analogous to friction angle (ϕ), α describes the angle from the p axis.

For our modeling, Mohr–Coulomb values of cohesion and friction angle were converted to Drucker–Prager values for input to the software using equations that assume the Drucker–Prager yield cone circumscribes the Mohr–Coulomb surface. This equivalence implies the conversion equations:

$$\alpha = \frac{2 \sin \varphi}{\sqrt{3}(3 - \sin \varphi)}, \qquad k = \frac{6c \cos \varphi}{\sqrt{3}(3 - \sin \varphi)}.$$

Tensile strength of rock is typically half of the cohesive strength (Price and Cosgrove, 1990), which is far smaller than that predicted by a Mohr–Coulomb failure envelope for typical rock friction angles. A limit on tensile strength, therefore, is usually added to the failure envelope. In the Mohr–Coulomb criterion, the simplest form of a limit comprises cutting the point off of the failure envelope along a vertical line (Fig. 20), equivalent to a minimum possible principal stress. In the Drucker–Prager criterion, the analogous limit is a minimum possible pressure, p. We set the tensile 'pressure' limit at half of the cohesion. Note that this pressure-type constraint allows the minimum principal stress to be more tensile than the tensile strength limit, as long as the maximum principal stress results in a pressure value above the limit.

Most of our models incorporated some amount of strain weakening. The weakening is defined by a decrease in friction angle and loss of cohesion, both over a specified interval of plastic strain. Values of friction angle and cohesion were converted to Drucker–Prager parameters for input in the modeling code. This weakening corresponds to narrowing the failure cone (decreased friction angle) and shifting the point of the cone to the origin in principal stress space (loss of cohesion). Plastic strain is measured as equivalent plastic strain, which is irreversible, and is defined as the summation of all of the incremental plastic strains without regard to the elastic strain. If the volumetric elastic strain is negligible, which will be true for most geological deformations, the equivalent plastic strain is the finite octahedral shear strain, which is a function of the second invariant of the finite strain tensor.

References

Armero, F., Garikipati, K., 1996. An analysis of strong discontinuities in multiplicative finite strain plasticity and their relation with the numerical simulation of strain localization in solids. International Journal of Solids and Structures 33, 2863–2885.

Aubertin, M., Servant, S., Gill, D.E., 1994. Experimental identification of kinematic and isotropic hardening in rocksalt. In: Nelson, P.P., Laubach, S.E. (Eds.). Rock Mechanics. Balkema, Rotterdam, pp. 723–730 Proceedings of the 1st North American Rock Mechanics Symposium.

Baars, D.L., 1962. Permian system of the Colorado Plateau. American Association of Petroleum Geologists Bulletin 46, 149–218.

Baars, D.L., Parker, J.W., Chronic, J., 1967. Revised stratigraphic nomenclature of Pennsylvanian system, Paradox Basin. American Association of Petroleum Geologists Bulletin 51, 393–403.

Baker, A.A., 1933. Geology and oil possibilities of the Moab district, Grand and San Juan Counties, Utah. U.S. Geological Survey Bulletin 841.

Banerdt, W.B., 1990. Horizontal stresses induced by vertical changes in the lithospheric column. Eos Transactions American Geophysical Union (Fall Meeting abstracts volume) 71, 1623.

Barnichon, J.D., Charlier, R., 1996. Finite element modelling of the competition between shear bands in the early stages of thrusting: strain localization analysis and constitutive law influence. In: Buchanan, P.C., Nieuwland, D.A. (Eds.). Modern Developments in Structural Interpretation, Validation and Modelling, pp. 235–250. Geological Society of London Special Publication 99.

Bazant, Z.P., Belytschko, T., 1987. Strain-softening continuum damage: localization and size effect. In: Desai, C.S., Krempl, E., Kiousis, P.D., Kundu, T. (Eds.). Constitutive Laws for Engineering Materials: Theory and Applications, Vol. 1. Elsevier, New York, pp. 11–33. Proceedings of the 2nd International Conference.

Belytschko, T., Bazant, Z.P., Hyun, Y.-W., Chang, T.-P., 1986. Strain softening materials and finite element solutions. Computers and Structures 23, 163–180.

Biggar, N.E., 1987. Quaternary studies in the Paradox Basin, southeastern Utah. Battelle Memorial Institute, Office of Nuclear Waste Isolation Technical Report ONWI-622, Columbus, OH.

Biggar, N.E., Adams, J.A., 1987. Dates derived from Quaternary strata in the vicinity of Canyonlands National Park. In: Campbell, J.A. (Ed.). Geology of Cataract Canyon and Vicinity, pp. 127–136. Four Corners Geological Society Guidebook, 10th Field Conference.

Bush, N.I., Harris, C., Grosfils, E.B., 1996. Refraction seismology in Devils Lane graben, Canyonlands National Park. Utah. Eos Transactions American Geophysical Union, Fall Meeting Supplement 77, F643.

Byerlee, J., 1978. Friction of rocks. Pure and Applied Geophysics 116, 615–626.

Cartwright, J.A., Mansfield, C.S., 1998. Lateral displacement variation and lateral tip geometry of normal faults in the Canyonlands National Park, Utah. Journal of Structural Geology 20, 3–19.

Cartwright, J.A., Trudgill, B.D., Mansfield, C.S., 1995. Fault growth by

segment linkage: an explanation for scatter in maximum displacement and trace length data from the Canyonlands grabens of SE Utah. Journal of Structural Geology 17, 1319–1326.

Cartwright, J.A., Mansfield, C.S., Trudgill, B.D., 1996. The growth of normal faults by segment linkage. In: Buchanan, P.C., Nieuwland, D.A. (Eds.). Modern Developments in Structural Interpretation, Validation and Modelling, pp. 163–177. Geological Society of London Special Publication 99.

Chen, W.-P., Han, D.J., 1988. Plasticity for Structural Engineers. Springer-Verlag, New York.

Condon, S.M., 1997. Geology of the Pennsylvanian and Permian Cutler Group and Permian Kaibab Limestone in the Paradox basin, southeastern Utah and southwestern Colorado. U.S. Geological Survey Bulletin 2000-P, 46.

Cundall, P.A., 1989. Numerical experiments on localization in frictional materials. Ingenieur-Archiv 59, 148–159.

Drucker, D.C., Prager, W., 1952. Soil mechanics and plastic analysis or limit design. Quarterly of Applied Mathematics 10, 157–165.

Elston, D.P., Shoemaker, E.M., 1961. Preliminary structure contour map on top of salt in the Paradox Member of the Hermosa Formation in the salt anticline region, Colorado and Utah. U.S. Geological Survey Oil and Gas Investigations Map, OM 209, scale 1:250,000.

Ely, R.W., 1987. Colluvium-filled fault fissures in the Needles fault zone, Cataract Canyon, Utah. In: Campbell, J.A. (Ed.). Geology of Cataract Canyon and Vicinity, pp. 69–73. Four Corners Geological Society Guidebook, 10th Field Conference.

Fung, Y.C., 1977. A First Course in Continuum Mechanics. 2nd ed. Prentice-Hall, Englewood Cliffs, NJ.

Garikipati, K., Hughes, T.J.R., 2000. A variational multiscale approach to strain localization-formulation for multidimensional problems. Computer Methods in Applied Mechanics and Engineering 188, 39–60.

Gerbault, M., Poliakov, A.N.B., Daignieres, M., 1998. Prediction of faulting from the theories of elasticity and plasticity: what are the limits? Journal of Structural Geology 20, 301–320.

Handin, J., 1966. Strength and ductility. In: Clark Jr, S.P. (Ed.). Handbook of Physical Constants, pp. 223–289. Geological Society of America Memoir 97.

Heiskanen, W.A., Vening Meinesz, F.A., 1958. The Earth and Its Gravity Field. McGraw-Hill, New York.

Hite, R.J., 1960. Stratigraphy of the saline facies of the Paradox Member of the Hermosa Formation of southeastern Utah and southwestern Colorado. Four Corners Geological Society Guidebook, 3rd Field Conference, pp. 86–89.

Hite, R.J., 1968. Salt deposits of the Paradox Basin, southeast Utah and southwest Colorado. Geological Society of America Special Paper 88, 319–330.

Hobbs, B.E., Mühlhaus, H.-B., Ord, A., 1990. Instability, softening and localization of deformation. In: Knipe, R.J., Rutter, E.H. (Eds.). Deformation Mechanisms, Rheology and Tectonics, pp. 143–165 Geological Society Special Publications 54.

Huntoon, P.W., 1982. The Meander anticline, Canyonlands, Utah: An unloading structure resulting from horizontal gliding on salt. Geological Society of America Bulletin 93, 941–950.

Huntoon, P.W., Billingsley, G.H., Breed, W.J., 1982. Geologic map of Canyonlands National Park and vicinity, Utah. Canyonlands Natural History Association, Moab, Utah, scale 1:62,500.

Jackson, M.P.A., 1995. Retrospective salt tectonics. In: Jackson, M.P.A., Roberts, D.G., Snelson, S. (Eds.). Salt Tectonics: a Global Perspective, pp. 1–28. American Association of Petroleum Geologists Memoir 65.

Jackson, M.P.A., Vendeville, B.C., 1994. Regional extension as a geologic trigger for diapirism. Geological Society of America Bulletin 106, 57–73.

Jackson, M.P.A., Vendeville, B.C., Schultz-Ela, D.D., 1994. Structural dynamics of salt systems. Annual Review of Earth and Planetary Sciences 22, 93–117.

Kenner, S., Segall, P., 1999. Time-dependence of the stress shadowing effect and its relation to the structure of the lower crust. Geology 27, 119–122.

Langford, R.P., Chan, M.A., 1989. Fluvial–aeolian interactions: Part II, ancient systems. Sedimentology 36, 1037–1051.

Lewis Sr, R.Q., Campbell, R.H., 1965. Geology and uranium deposits of Elk Ridge and vicinity, San Juan County, Utah. U.S. Geological Survey Professional Paper 474-B, 69.

Lundin, E.R., 1992. Thin-skinned extensional tectonics on a salt detachment, northern Kwanza Basin, Angola. Marine and Petroleum Geology 9, 405–411.

Mandl, G., 1988. Mechanics of Tectonic Faulting. Elsevier, Amsterdam.

Marone, C., 1998. Laboratory-derived friction laws and their application to seismic faulting. Annual Reviews of Earth and Planetary Sciences 26, 643–696.

McCleary, J.R., Romie, J.E., 1986. Stratigraphic and structural configuration of the Navajo (Jurassic) through Ouray (Mississippian–Devonion) Formations in the vicinity of Davis and Lavender Canyons, southeastern Utah, Battelle Memorial Institute, Office of Nuclear Waste Isolation Technical Report ONWI-594, Columbus, OH.

McGarr, A., 1988. On the state of lithospheric stress in the absence of applied tectonic forces. Journal of Geophysical Research 93B, 13609–13617.

McGill, G.E., Stromquist, A.W., 1974. A model for graben formation by subsurface flow; Canyonlands National Park, Utah. University of Massachusetts, Amherst, Department of Geology and Geography, Contribution 15.

McGill, G.E., Stromquist, A.W., 1975. Origin of graben in the Needles District, Canyonlands National Park, Utah. In: Fassett, J.E. (Ed.). Canyonlands Country, pp. 235–243. Four Corners Geological Society Guidebook, 8th Field Conference.

McGill, G.E., Stromquist, A.W., 1979. The grabens of Canyonlands National Park, Utah — geometry, mechanics, and kinematics. Journal of Geophysical Research 84, 4547–4563.

McGill, G.E., Schultz, R.A., Moore, J.M., 2000. Fault growth by segment linkage: an explanation for scatter in maximum displacement and trace length data from the Canyonlands grabens of SE Utah: discussion. Journal of Structural Geology 22, 135–140.

Melosh, H.J., Williams, C.A., 1989. Mechanics of graben formation in crustal rocks: a finite element analysis. Journal of Geophysical Research 94B, 13961–13973.

Moore, J.M., Schultz, R.A., 1996. Mechanisms for graben growth: evidence from fossil and active relay-ramps at Canyonlands National Park, Utah. Eos Transactions American Geophysical Union, Fall Meeting Supplement 77, F643.

Moore, J.M., Schultz, R.A., 1999. Processes of faulting in jointed rocks of Canyonlands National Park, Utah. Geological Society of America Bulletin 111, 808–822.

Moore, J.M., Schultz, R.A., Grosfils, E.B., Fori, A.N., Roadarmel, W.H., Bush, N.I., Harris, C., Ivers, C.B., 1997. The 1995 Canyonlands initiative: field study of small planetary grabens. Lunar and Planetary Science Conference 28, 975–976.

Munson, D.E., DeVries, K.L., 1991. Development and Validation of a Predictive Technology for Creep Closure of Underground Rooms in Salt. Balkema, Rotterdam, pp. 127–134. Proceedings 7th International Congress on Rock Mechanics.

Needleman, A., 1988. Material rate dependence and mesh sensitivity in localization problems. Computer Methods in Applied Mechanics and Engineering 67, 69–85.

Needleman, A., Tvergaard, V., 1984. Finite element analysis of localization in plasticity. In: Oden, J.T., Carey, G.F. (Eds.). Finite Elements — Special Problems in Solid Mechanics, vol. 5. Prentice-Hall, Englewood Cliffs, NJ, pp. 94–157.

Pfeifle, T.W., Mellegard, K.D., Senseny, P.E., 1983. Constitutive properties of salt from four sites, Battelle Memorial Institute, Office of Nuclear Waste Isolation Technical Report ONWI-314, Columbus, Ohio.

Pietruszczak, St., Mróz, Z., 1981. Finite element analysis of deformation of

strain-softening materials. International Journal for Numerical Methods in Engineering 17, 327–344.

Potter Jr, B.P., McGill, G.E., 1978. Valley anticlines of the Needles District, Canyonlands National Park, Utah. Geological Society of America Bulletin 89, 952–960.

Price, N.J., Cosgrove, J.W., 1990. Analysis of Geological Structures. Cambridge University Press, Cambridge.

Pusch, R., 1995. Rock Mechanics on a Geological Base. Elsevier, Amsterdam Developments in Geotechnical Engineering 77.

Rice, J.R., 1977. The localization of plastic deformation. In: Koiter, W.T. (Ed.). Theoretical and Applied Mechanics. North-Holland, Amsterdam, pp. 207–220. Proceedings 14th International Congress of Theoretical and Applied Mechanics.

Rudnicki, J.W., Rice, J.R., 1975. Conditions for the localization of deformation ure-sensitive dilatant materials. Journal of the Mechanics and Physics of Solids 25, 371–394.

Schultz, R.A., 1996. Relative scale and the strength and deformability of rock masses. Journal of Structural Geology 18, 1139–1149.

Schultz, R.A., Moore, J.M., 1996. New observations of grabens from the Needles District, Canyonlands National Park, Utah. In: Huffman Jr, A.C., Lund, W.R., Godwin, L.H. (Eds.). Geology and Resources of the Paradox Basin, pp. 295–302. Utah Geological Association Guidebook 25.

Schultz-Ela, D.D., Jackson, M.P.A., 1996. Relation of subsalt structures to suprasalt structures during extension. American Association of Petroleum Geologists Bulletin 80, 1896–1924.

Senseny, P.E., Hansen, F.D., Russell, J.E., Carter, N.L., Handin, J.W., 1992. Mechanical behaviour of rock salt: phenomenology and micromechanisms. International Journal of Rock Mechanics and Mining Sciences and Geomechanics Abstracts 29, 363–378.

Sluys, L.J., de Borst, R., 1991. Solution methods for localization in fracture dynamics. In: van Mier, J.G.M., Rots, J.G., Bakker, A. (Eds.). Fracture Processes in Concrete, Rock and Ceramics. E. & F.N. Spon, London, pp. 661–671.

Stromquist, A.W., 1976. Geometry and growth of grabens, Lower Red Lake Canyon area, Canyonlands National Park, Utah. University of Massachusetts, Amherst, Department of Geology and Geography, Contribution 28.

Trudgill, B., Cartwright, J.A., 1994. Relay-ramp forms and normal-fault linkages, Canyonlands National Park, Utah. Geological Society of America Bulletin 106, 1143–1157.

Turcotte, D.L., Schubert, G., 1982. Geodynamics: Applications of Continuum Physics to Geological Problems. John Wiley & Sons, New York.

Tvergaard, V., Needleman, A., Lo, K.K., 1981. Flow localization in the plane strain tensile test. Journal of the Mechanics and Physics of Solids 29, 115–142.

Van Keken, P.E., Spiers, C.J., Van den Berg, A.P., Muyzert, E.J., 1993. The effective viscosity of rocksalt: implementation of steady-state creep laws in numerical models of salt diapirism. Tectonophysics 225, 457–476.

Vardoulakis, I., Sulem, J., 1995. Bifurcation Analysis in Geomechanics. Blackie, London.

Vendeville, B.C., 1987. Champs de failles et tectonique en extension: modélisation expérimentale: Mémoires du Centre Armoricain d'Etudes Structurales des Socles No. 15, Rennes, France.

Vendeville, B.C., Jackson, M.P.A., 1992. The rise of diapirs during thin-skinned extension. Marine and Petroleum Geology 9, 331–353.

Vermeer, P.A., 1990. The orientation of shear bands in biaxial tests. Géotechnique 40, 223–236.

Weijermars, R., Schmeling, H., 1986. Scaling of Newtonian and non-Newtonian fluid dynamics without inertia for quantitative modelling of rock flow due to gravity (including the concept of rheological similarity). Physics of the Earth and Planetary Interiors 43, 316–330.

Weijermars, R., Jackson, M.P.A., Vendeville, B.C., 1993. Rheological and tectonic modelling of salt provinces. Tectonophysics 217, 143–174.

Woodward–Clyde Consultants, 1982. Geologic characterization report for the Paradox Basin study region, Utah study areas, Battelle Memorial Institute, Office of Nuclear Waste Isolation Technical Report ONWI-290, Columbus, OH.

Woodward–Clyde Consultants, 1983. Overview of the regional geology of the Paradox Basin study region, Battelle Memorial Institute, Office of Nuclear Waste Isolation Technical Report ONWI-92, Columbus, OH.